Assessment of Graphitized Coal Ash Char Concentrates as a Potential Synthetic Graphite Source

Charlotte Badenhorst [1,*], **Cláudia Santos [2]**, **Juan Lázaro-Martínez [3]**, **Barbara Białecka [4]**,
Mihai Cruceru [5], **Alexandra Guedes [2]**, **Renato Guimarães [2]**, **Karen Moreira [2]**,
Georgeta Predeanu [6], **Isabel Suárez-Ruíz [7]**, **Ignacio Cameán [7]**, **Bruno Valentim [2]**
and Nicola Wagner [1]

1   DSI-NRF CIMERA, Department of Geology, University of Johannesburg, PO Box 524, Auckland Park,
    Johannesburg 2006, South Africa; nwagner@uj.ac.za
2   Earth Science Institute–Porto Pole, Department of Geosciences, Environment and Spatial Plannings,
    Faculty of Sciences, University of Porto, rua do Campo Alegre s/n, 4169-007 Porto, Portugal;
    anasantos@fc.up.pt (C.S.); aguedes@fc.up.pt (A.G.); renatotatas@gmail.com (R.G.);
    karen.moreira@fc.up.pt (K.M.); bvvalent@fc.up.pt (B.V.)
3   Departamento de Química Orgánica, Facultad de Farmacia y Bioquímica, Universidad de Buenos Aires,
    IQUIMEFA-UBA-CONICET, Junín 956, CABA, Argentina; jmlazaromartinez@gmail.com
4   Główny Instytut Górnictwa, Central Mining Institute (GIG), plac Gwarków 1, 40-166 Katowice, Poland;
    bbialecka@gig.eu
5   Engineering Faculty, University Constantin Brancusi of Targu Jiu, Republicii 1, 210152 Targu Jiu, Romania;
    cruceru.mihai@gmail.com
6   Research Center for Environmental Protection and Eco-Friendly Technologies (CPMTE),
    University Politehnica of Bucharest, Polizu 1, Sector 1, 011061 Bucharest, Romania; gpredeanu@gmail.com
7   Instituto de Ciencia y Tecnología del Carbono (INCAR-CSIC), c./Francisco Pintado Fe 26,
    33011 Oviedo, Spain; isruiz@incar.csic.es (I.S.-R.); icamean@incar.csic.es (I.C.)
*   Correspondence: charlotte.cb82@gmail.com; Tel.: +27-115-594-719

check for
updates

Abstract: Coal ash char concentrates from four countries (Portugal, Poland, Romania, and South Africa) were prepared, characterised, and graphitized under the scope of the Charphite project (Third ERA-MIN Joint Call (2015) on the Sustainable Supply of Raw Materials in Europe). Coal ash chars may be a secondary raw material to produce synthetic graphite and could be an alternative to natural graphite, which is a commodity with a high supply risk. The char concentrates and the graphitized material derived from the char concentrates were characterised using proximate analysis, X-ray fluorescence, X-ray diffraction (structural), Raman microspectroscopy, solid-state nuclear magnetic resonance, scanning electron microscopy, and petrographic analyses to determine if the graphitization of the char was successful, and which char properties enhanced or hindered graphitization. Char concentrates with a lower proportion of anisotropic particles and a higher proportion of mixed porous particles showed greater degrees of graphitization. It is curious to see that embedded Al_2O_3 minerals, such as glass and clay, influenced graphitization, as they most likely acted as catalysts for crystal growth in the basal direction. However, the graphitized samples, as a whole, do not compare well against a reference natural graphite sample despite some particles in select char concentrates appearing to be graphitized following graphitization.

Keywords: Charphite; catalytic graphitization; crystallite growth; natural graphite; microtexture

1. Introduction

Approximately 1222 million tons of coal combustion by-products (CCP), such as bottom ash (CBA), fly ash (CFA), and flue gas desulphurization residues (FGD), are produced annually in the world [1].

The landfilling thereof leads to environmental, health, and economic concerns [2,3]. The mechanisms of ash formation are complicated and consist of the melting, agglomeration, reaction, and solidification of the minerals hosted in the coal precursor (kaolinite, illite, calcite, dolomite, siderite, quartz, and pyrite, amongst others). CFA and CBA consist of aluminosilicate amorphous phases and minerals, such as quartz, mullite, hematite, magnetite, and lime. In CBA, anorthite is also frequently found. Due to the rapid cooling of molten ash, crystallization is hindered, explaining the high percentages of amorphous material in CFA and CBA. Char, a carbon-rich solid residue occurring as partially or incomplete reacted carbon, is also present in CFA and CBA in percentages <45% [4]. Where civil construction activities occur in the proximity of coal thermoelectric power plants (CTPP), the use of CCP is viable, and CFA and FGD are consumed in concrete and plasterboard production, respectively [5]. Nevertheless, innovative and new solutions are constantly sought for re-using CFA and CBA, especially when high carbon contents preclude its utilization in the concrete industry.

Char is a value-added component in ash that can be extracted and utilised [6]. Char is generally a highly porous material, making it ideal for mercury adsorption and activated carbon applications [7–12]. It has a high degree of turbostratic structural order and a lamellar microtexture [4,13–17], hence its potential as a secondary raw material to produce synthetic graphite that could be an alternative to natural graphite.

Natural graphite is listed by the European Union and the United States as a critical raw material (CRM), with a high supply risk and economic importance [18,19]. The critical status is largely due to the increase in graphite demand globally, for usage in high cost applications, such as lithium-ion batteries, fuel cells, and pebble-bed nuclear reactors. Natural graphite recycling and substitution are two important ways to reduce graphite supply risk. However, the recycling of graphite is limited (e.g., electrodes may be recycled), and only in a few applications can the graphite be recovered due to low economic incentive and technical challenges. In addition, in some applications (e.g., brakes), graphite becomes dispersed in the environment, constituting a source of pollution [20].

Research is scarce on the potential of using coal ash char as a secondary raw material for synthetic graphite production [21–23]. Cabielles et al. [21,22] graphitized coal ash char from a CTPP burning anthracite coal, and the resultant graphitized material compared well to their reference commercial synthetic graphite. The authors also investigated the influence of graphitization temperature and the mineral matter content in the coal ash char on the graphitization process. Regarding the graphitization temperature, structural analyses showed that graphitization is achieved at 2400 °C. However, structural analyses were unable to differentiate between carbon structures with different degrees of order. When using imaging analyses, the appearance of lamellar microtexture graphite in some individual particles heated to higher than 2400 °C suggests that graphitization can progress well beyond this temperature. Regarding the influence of mineral matter in the coal ash char, Cabielles et al. [21,22] found that mineral matter had a counter effect on graphitization. On the one hand, mineral matter preferentially promoted the coalescence of crystallites along the a-axis. On the other hand, this coalescence facilitated the flattening of pores, thus decreasing the breakage temperature, which led to structural evolution only noticeable by a slow vegetative growth of crystallites along the a-axis.

The idea that mineral matter in graphite precursors can act as catalysts during graphitization gained interest in the 1970s (e.g., [24]). Pappano and Schobert [25] and González et al. [26], amongst others, investigated the matter further and suggested that it is the formation and subsequent decomposition of carbides that lead to better graphitization. Metals in minerals (such as Si, Al, Ti, Ca, Mg, Mn, and Fe) react with thermodynamically unstable and disorganized carbon (sp^3 C) in boundaries of turbostratic domains to form carbides. The carbides decompose to leave an organized graphite structure behind, which increases the size of the crystallites along the a-axis. González et al. [26] state that potassium and iron metals in minerals such as illite, ankerite, and siderite are the main active catalysts during the graphitization of anthracite coal. Pappano and Schobert [25] determined that silicon in anthracite forms silicon carbide, which decomposes and enhances graphitization. Cabielles [22] also noted that

silicon carbide decomposes to form ordered graphite in coal ash char; however, the authors also suggested that iron carbide also influences the graphitization process. Aluminosilicate minerals are effective catalysts, especially in the presence of iron [27,28]. Lastly, González et al. [26] observed that mineral matter finely interwoven in the structure of a carbonaceous precursor will enhance the catalytic effect. The initial anisotropic-like microtexture and the pore shape are also known to influence the graphitization process [25]. A preferential lamellar microtexture of the polyaromatic basic structural units (BSUs) allows for bond-breaking and coalescence during graphitization (a description of this process is provided by Rouzaud and Oberlin [29] and Oberlin [30]). González et al. [31] determined that samples with a lower starting anisotropic percentage lead to a better structure with a higher percentage of anisotropic particles after carbonisation, and a higher anisotropic percentage after carbonisation lead to better graphitization. Suárez-Ruiz and García [32] also concluded that crystalline aggregates, microspheres, and flake microstructures, commonly found in natural graphite, are more frequently observed in graphitized material obtained from carbonised anthracite material with a larger degree of textural anisotropy. Furthermore, pore rupturing and flattening during graphitization enhances the graphitization process [33–36]. Dense and massive particles have been shown to graphitize better than highly porous material [32].

The results presented here form part of the third ERA-MIN collaboration (2015) on Sustainable Supply of Raw Materials in Europe: "Coal char as a substituting material of natural graphite in green energy technologies–Charphite" (https://www.fc.up.pt/charphite/). Partners from Portugal, Poland, Romania, Argentina, Spain, and South Africa are involved in this collaboration to assess the feasibility of using coal ash char as a secondary raw material to form synthetic graphite and to test its application in electrocatalysis reactions (Figure 1). The first stages of sample selection, coal and ash characterisation and char concentration, were reported previously [37–43] (including the testing of char-poor ash residue in building applications [44].
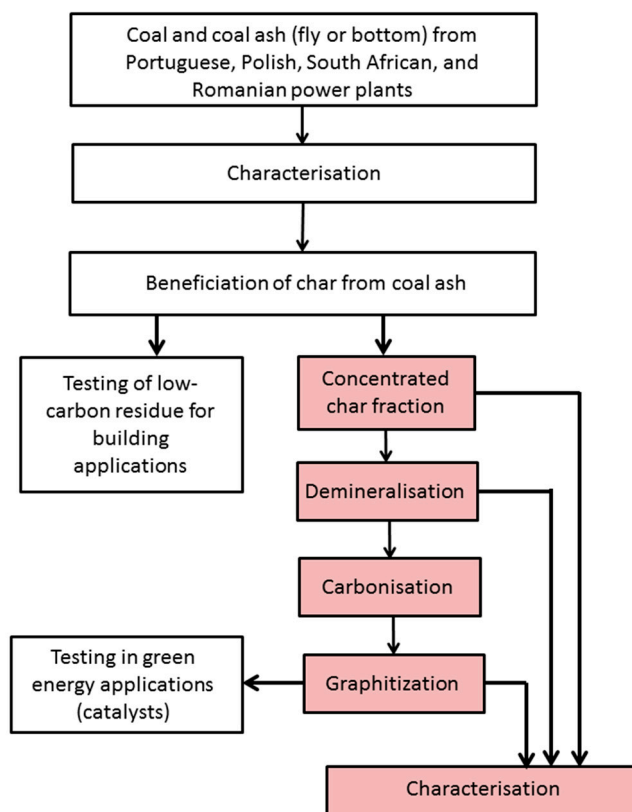

Figure 1. Charphite project methodology (aspects covered in the current paper are shaded).

In this paper, the results from the characterisation of the char concentrates (char concentrates and demineralised char concentrates) and the graphitized material are presented. A series of analytical techniques were used: proximate analysis; X-ray fluorescence (XRF) for major oxides determination; X-ray diffraction (XRD) for structural characterisation; Raman microspectroscopy to characterise structural ordering; solid-state nuclear magnetic resonance (ss-NMR) experiments in order to study both the graphitic and aliphatic contents at the atomic level in the different samples; and scanning electron microscopy with energy dispersive spectroscopy (SEM/EDS) and petrography analyses for morphotypes quantification and qualification, detailed imaging and new formed materials identification. The results of these analyses were used to determine if the graphitization of the char was successful (a natural graphite sample was used as a reference material), and which char properties most likely enhanced or hindered graphitization.

2. Materials and Methods

2.1. Samples, Demineralisation, Carbonisation, and Graphitization

Coal, CFA, and CBA samples were supplied by Portuguese, Polish, South African, and Romanian CTPPs. The samples were characterised in detail [37,40], and selected ash samples were beneficiated to obtain a char concentrate product with a high carbon grade. The beneficiation process differed for each country [38,39,41–43], and some resulting low-carbon residues were tested for applications in building materials [44]. The concentrated char fractions were characterised in detail, and some results were already presented in Badenhorst et al. [37]. Before the graphitization trials commenced, the char concentrates were demineralised (to remove remaining carbonates and silicates and avoid the clogging of the graphitization chamber) and then carbonised to remove volatiles, which is a necessary step before the process of graphitization (e.g., [45]). The carbonisation and graphitization trials were carried out at Instituto de Ciencia y Tecnología del Carbono (INCAR), Oviedo, Spain. A natural graphite sample from South Africa was used as a reference for the graphitized material. The sample identification is presented in Table 1, and the characterisation techniques used are summarised in Table 2.

Table 1. Sample nomenclature and information (C—Char concentrates, CD—Demineralised char concentrates, CD-G—Graphitized demineralised char concentrates, NG—Natural graphite, PT—Portugal, PL—Poland, SA—South Africa, RO—Romania, CFA—Coal fly ash, CBA—Coal bottom ash, CTPP—Coal thermoelectric power plant).

Sample Type	Sample Nomenclature	Sample Information
Portugal Char concentrate Demineralised char concentrate Graphitized demineralised char concentrate	 C-PT CD-PT CD-PT-G	CFA sample from the Pegop CTPP, concentrated via a combination of dry sieving, gravimetric separation, wet sieving, dry impaction, elutriation, and magnetic separation. The fixed carbon of the char concentrate was 75.1 wt. %.
Poland Char concentrate Demineralised char concentrate Graphitized demineralised char concentrate	 C-PL CD-PL CD-PL-G	CBA sample from the Elektrownia Siersza CTPP, concentrated via a combination of dry sieving, a rising water stream, and magnetic separation. The fixed carbon of the char concentrate was 70.1 wt. %.
South Africa Char concentrate Demineralised char concentrate Graphitized demineralised char concentrate	 C-SA CD-SA CD-SA-G	CFA sample from an Eskom CTPP, concentrated via a combination of dry sieving, double stage electrostatic separation, and magnetic separation. The fixed carbon of the char concentrate was 74.7 wt. %.
Romania Char concentrate Demineralised char concentrate Graphitized demineralised char concentrate	 C-RO CD-RO CD-RO-G	CBA sample from the Govora CTPP, concentrated via a combination of dry sieving, gravimetric separation, magnetic separation, and grinding followed by sieving. The fixed carbon of the char concentrate was 59.2 wt. %.
Natural graphite	NG-SA	Flake graphite from the Goedehoop deposit, Limpopo Province, South Africa.

Table 2. Characterisation techniques (XRF—X-ray fluorescence, XRD—X-ray diffraction, ss-NMR—Solid-state nuclear magnetic resonance, SEM/EDS—Scanning electron microscopy with energy dispersive spectroscopy).

Sample Type	Proximate	XRF	XRD (Structural)	Raman Microspectroscopy	ss-NMR	SEM/EDS	Petrography
C			×	×		×	×
CD	×	×			×	×	
CD-G			×	×		×	×
NG			×	×			×

×—Characterisation technique applied to the sample type.

For the char demineralisation, ten grams of char concentrate was placed in a 1 L Teflon bottle and treated sequentially with HCL and HF. An amount of 250 mL of HCL (20%) was added to the sample in the Teflon bottle, and the bottle was agitated in a Sky Line Shaker Dos-20L for 18 h. The sample was rinsed with distilled water ($\approx$750 mL) and filtrated. An amount of 150 mL of HF (40%) was added to the sample, and the bottle was agitated on the shaker table for 18 h, followed by rinsing and filtration of the sample. The HCL step was repeated, followed by two-stage rinsing and filtration, and dried at 80 °C until it reached a constant weight.

The carbonisation of the demineralised char concentrates was made at 1000 °C in a Carbolite horizontal tube furnace (CTF model) under argon flow (50 mL/min), at a heating rate of 2 °C and a residence time of 1 h. The samples were cooled to room temperature inside the furnace under argon. The samples were weighed before and after the carbonisation process to determine the weight loss during the process.

The graphitization trials by high-temperature thermal treatments (HTT) were conducted in a Xerion three-phase electric furnace with the software Eurotherm 2704 (KD485, Eurotherm, Worthing, UK). The heating rate, residence time, and the cooling of the furnace were controlled. The furnace is equipped with a graphite heating and insulation system in water-cooled double-wall vessels, with an optical pyrometer (Keller model PZ 30, Keller, Ibbenbüren, Germany) able to measure temperatures up to 3000 °C. The samples were placed in graphite crucibles and heated to a temperature of 2600 °C in the graphite furnace, under argon flow, at heating rates of 50 °C/min, 100 °C/min, 25 °C/min, and 10 °C/min in the temperature intervals of 20–700 °C, 700–1000 °C, 1000–2000 °C, and 2000–2600 °C, respectively. The samples were kept at the maximum temperature (2600 °C) for 1 h. These experimental conditions were selected based on previous work by González et al. [26,31,45,46]. Cabielles et al. [21,22] graphitized coal ash char obtained from a CTPP burning anthracite coal. They found that graphitization is seemingly completed at 2400 °C; however, imaging analyses showed that there are still some individual particles that were not graphitized and may continue to graphitize above 2400 °C. Therefore, we have chosen 2600 °C to ensure complete graphitization in our study.

2.2. Sample Characterisation

The proximate analysis was carried out according to ISO standards to determine the moisture [47], ash [48], and volatile matter [49] contents, and the fixed carbon (FC) was calculated by difference.

The XRF analysis was carried out at Bureau Veritas Commodities Canada Ltd. (Vancouver, BC, Canada) using lithium tetraborate fusion to digest the samples.

XRD diffractograms, to determine the structural ordering, were recorded at INCAR (Oviedo, Spain) on a Bruker D8 Advance powder diffractometer (Bruker, Billerica, MA, USA) equipped with a monochromatic Cu KαX-ray source and an internal silicon powder standard. The XRD analysis was conducted to determine the carbon structural order and crystalline parameters of the samples and not the mineralogy of the samples. The mineral spectrum and the structural spectrum obtained by XRD are not the same, nor obtained with the same measurement program and conditions. Diffraction data were collected by step scanning using a step size of 0.02° 2θ and a scan step of 2 s. For each sample, three diffractograms were obtained, employing a different representative batch of samples for each run.

The mean interlayer spacing, d_{002}, was determined from the position of the (002) peak by applying Bragg's equation (Equation (1)). The crystallite sizes, L_c and L_a, were calculated by measuring the full width at half maximum (FWHM) of the (002) and (110) peaks, respectively, and by applying Scherrer's equation (Equation (2)). The average number of aromatic layers <N> in the stack was determined following the procedure described by Laggoun-Defarge et al. [50] (Equation (3)). The graphitization degree (GD) was also determined (Equation (4)). The broadening of the diffraction peaks due to instrumental factors was corrected by using a silicon standard. The d_{002} values show standard errors lower than 0.1%.

$$d_{002} = \frac{\lambda}{2\sin\theta} \tag{1}$$

$$L = \frac{K\lambda}{\beta\cos\theta} \tag{2}$$

$$<N> = \frac{L_c}{d_{002}} \tag{3}$$

$$GD = \frac{0.3440(nm) - d_{002}}{0.3440(nm) - 0.3354(nm)} \times 100 \tag{4}$$

In the equations above, K is a coefficient (0.89 for L_c and 1.84 for L_a), λ is the X-ray wavelength, θ is Bragg's angle (peak position), and β is the broadening of the diffraction peak measured at its FWHM (in radians) [51].

Blocks for Raman microspectroscopy were prepared by mounting the samples in epoxy resin and polishing them following ISO 7404-2 [52]. Polishing can lead to an increase in observed Raman disorder at the block surface; therefore, all spectra were acquired at a penetration depth larger than 5 nm. For spectral acquisition, a WITec Alpha300 R confocal Raman microspectrometer (housed at the University of Johannesburg Assore Raman Laboratory) was used. The microspectrometer was calibrated with a silicon standard before spectral acquisition commenced. Measurements were obtained at room temperature using a 532 nm wavelength of a frequency-doubled solid-state YAG laser source at a laser strength of 3.5 W. The low laser strength was chosen to avoid sample damage and the shifting of peaks. Objective lenses from 20× to 50× were used. The integration time was set at 30 s with a total of five cycles and with scans extending from 0 to 3600 cm^{-1}. Ten to 25 spectra were randomly obtained from each sample. These spectra were taken from different particles in the blocks, as well as different spots in individual particles. OriginPro 2020 software (OriginLab Corporation, Northampton, MA, USA) was used for curve fitting of the 1st order spectra. For the char concentrates, the background due to fluorescence was subtracted by using a 4th order polynomial function. A polynomial baseline is preferred over a linear baseline, due to the overestimation of the band intensities from the latter [53]. The D1, G, and D4 bands were fitted with a Gaussian function, and the D2 and D3 bands with a Lorentzian function. Restrictive bounds were added (as suggested by Sforna et al. [54]) to converge appropriately. The R^2 values for all fitted curves were >0.999. For the graphitized demineralised char concentrates and the reference natural graphite sample, the background due to fluorescence was subtracted by using a linear function. A linear baseline is preferred, due to the overestimation of the band intensities from a polynomial baseline. The D1, G, D2, and D4 bands were fitted with a Lorentzian function and the D3 band with a Gaussian function. The R^2 values for all fitted curves were >0.998. Once all spectra were fitted, the average band position, average FWHM, average band area, and average band intensity were obtained. To determine the error, the standard deviations were considered. Furthermore, the distance between the G and D1 bands, the FWHM ratio between the D1 and G bands, the area ratio between the D1 and G bands, and the RA1 (Equation (5)) and RA2 (Equation (6)) values were calculated for the char concentrates, following Schito et al. [53], Sforna et al. [54], Baludikay et al. [55], and Lahfid et al. [56]. These calculated parameters are frequently used to indicate maturity in disorganised carbonaceous material. For the graphitized demineralised char concentrates and the reference natural graphite sample, the total intensity ratio (Equation (7))

was used, as suggested by Cabielles et al. [21,22] and González et al. [26,31,45,46]. This calculated parameter is frequently used to indicate maturity in organised carbonaceous material.

$$RA1 = \frac{A_{D1} + A_{D4}}{A_{D1} + A_{D2} + A_{D3} + A_{D4} + A_G} \tag{5}$$

$$RA2 = \frac{A_{D1} + A_{D4}}{A_{D2} + A_{D3} + A_G} \tag{6}$$

$$I_t = \frac{I_{D1}}{I_{D1} + I_{D2} + I_G} \tag{7}$$

ss-NMR data were acquired with a Bruker Avance-III HD spectrometer equipped with a 14.1 T narrow bore magnet operating at Larmor frequencies of 600.09 MHz and 150.91 MHz for ^{1}H and ^{13}C, respectively (IQUIMEFA, Argentina and Universidad de Málaga, Spain). Powdered samples were packed into 3.2 or 2.5 mm ZrO_2 rotors and rotated at room temperature at magic angle spinning (MAS) rates of 15 or 32 kHz, respectively. Cross-polarization and magic angle spinning (^{13}C-CP-MAS) experiments were done in a 3.2 mm MAS probe. Glycine was used as an external reference compound for the recording of the ^{13}C spectra and to set the Hartmann−Hahn matching condition in the CP-MAS experiments in ^{13}C spectra. The contact time during CP was 2000 μs. The small phase incremental alternation with 64 steps (SPINAL64) sequence was used for heteronuclear decoupling during acquisition. ^{13}C natural abundance direct polarization experiments (^{13}C DP) with proton decoupling (SPINAL64) during acquisition were conducted. An excitation pulse of 4.0 μs and a recycling time of 60 s were used, and 8000 scans were accumulated to obtain quantitative and good signal-to-noise ratios. ^{1}H-MAS ss-NMR spectra were recorded in a 2.5 mm MAS probe using single pulse excitation experiments. Chemical shifts for ^{1}H (in ppm) are relative to $(CH_3)_4Si$. The ^{1}H MAS ss-NMR analyses were only conducted on the demineralised char concentrate samples as the signal-to-noise ratio in the char concentrate samples was too low.

The SEM/EDS analysis was performed at the Materials Centre of the University of Porto (CEMUP, Portugal) using an FEI Quanta 400 FEGESEM/EDAX Genesis X4M. The equipment was operated at 15 kV in high vacuum mode with a manual aperture and an instrument-specific 4.5 beam spot size setting. The samples (powder and polish blocks) were sputter-coated to form a thin carbon film. The backscattered electron (BSE) detector mode was preferentially used to identify and characterise the inorganic phases, due to its capability to discriminate elements based on the atomic weight. The secondary electron (SE) was mainly used to study the particle morphology, especially in the powder samples. Semiquantitative chemical analyses were performed via X-ray microanalysis (EDS).

The same blocks used for Raman microspectroscopy were repolished and used for the petrographic analysis. A ZEISS AxioImager M2M reflected light microscope, housed at the University of Johannesburg, Department of Geology, was used. The morphological composition of the char concentrate samples was determined by using the classification methods proposed by Hower [57] and the International Committee for Coal and Organic Petrology (ICCP) char classification [58]. Only photographs were taken for the graphitized demineralised char concentrates and the reference natural graphite. Photographs were taken in colour and monochrome polarized light using the x50 oil immersion lens.

3. Results

3.1. Characterisation of Char Concentrates

A summary of the earlier published char concentrate characterisation results is provided in Table 3 (after Badenhorst et al. [37]).

For the char concentrate samples (Figure 2A), the diffractograms are diffused, the three-dimensional reflection peaks are absent, and the 002 peaks are asymmetrical, which indicates that aliphatic

compounds, opposed to aromatic compounds, are dominant in the samples [59–65]). The d_{002}, L_c, and <N> for each char concentrate are provided in Table 4.

Table 3. Summary of earlier published char concentrate characterisation results [37]. Refer to Table 1 for sample description (a.d.b—air-dried basis).

	Analysis	C-PT	C-PL	C-SA	C-RO
Proximate Analysis (a.d.b wt. %)	Moisture	0.5	3.3	3.6	7.6
	Ash yield	22.4	22.2	17.7	13.6
	Volatile matter	2.0	4.4	4.0	19.6
	Fixed carbon	75.1	70.1	74.7	59.2
Ultimate Analysis (a.d.b wt. %)	Total sulphur	0.32	0.36	0.30	1.29
	Carbon content	74.50	70.70	75.00	67.10
	Hydrogen content	0.37	0.28	0.18	1.70
	Nitrogen content	0.98	0.90	1.11	0.56
	Oxygen content	0.93	2.26	2.11	8.15
Carbon form Analysis (wt. %)	Total carbon	75.37	74.54	75.45	69.50
	Elemental carbon	69.83	56.30	66.58	3.30
	Organic carbon	4.12	14.01	7.18	63.10
	Inorganic carbon	1.42	4.23	1.69	3.10
XRD Analysis (wt. %)	Quartz (SiO_2)	2.4	1.1	2.0	0.4
	Mullite ($3Al_2O_32SiO_2/2Al_2O_3SiO_2$)	5.6	5.1	6.6	0.9
	Gypsum ($CaSO_4 \cdot 2H_2O$)	0.0	0.0	0.1	0.1
	Calcite ($CaCO_3$)	0.0	0.6	0.0	0.5
	Bassanite ($CaSO_4 \cdot 0.5H_2O/2CaSO_4 \cdot H_2O$)	0.0	0.0	0.0	0.4
	Amorphous	92.0	93.2	91.4	97.7
XRF Analysis (wt. %)	SiO_2	16.12	10.90	23.93	4.11
	Al_2O_3	7.13	6.12	11.21	1.88
	Fe_2O_3	1.03	0.77	0.82	1.19
	CaO	0.32	1.47	0.79	3.11
	MgO	0.17	1.00	0.17	0.36
	Na_2O	0.18	0.30	0.04	<0.01
	K_2O	0.45	0.51	0.25	0.16
	SO_3	0.19	0.15	0.35	0.72
	MnO	<0.01	<0.01	<0.01	<0.01
	TiO_2	0.21	0.23	0.56	0.08
	P_2O_5	0.04	0.04	0.14	0.02
	Cr_2O_3	<0.01	<0.01	<0.01	<0.01
	Loss on Ignition	73.43	77.64	61.51	87.64

XRD, Raman microspectroscopy, SEM/EDS, and petrography results are provided in this paper. The XRD diffractograms are provided in Figure 2.

Table 4. XRD crystallite size results (d_{002}—mean interlayer spacing, L—crystallite size, N—average number of aromatic layers, GD—graphitization degree).

Sample Nomenclature	d_{002} (nm)	La (nm)	Lc (nm)	<N>	GD (%)
C-PT	0.3542	n.d	1.9	5	-
C-PL	0.3673	n.d	1.3	4	-
C-SA	0.3595	n.d	1.4	4	-
C-RO	0.3773	n.d	1.2	3	-
CD-PT-G	0.3423	24.4	9.3	27	19.77
CD-PL-G	0.3394	46.8	10.7	32	53.49
CD-SA-G	0.3360	98.7	44.6	133	93.02
CD-RO-G	0.3371	50.7	22.2	66	80.23
NG-SA	0.3347	213.2	33.9	101	108.14

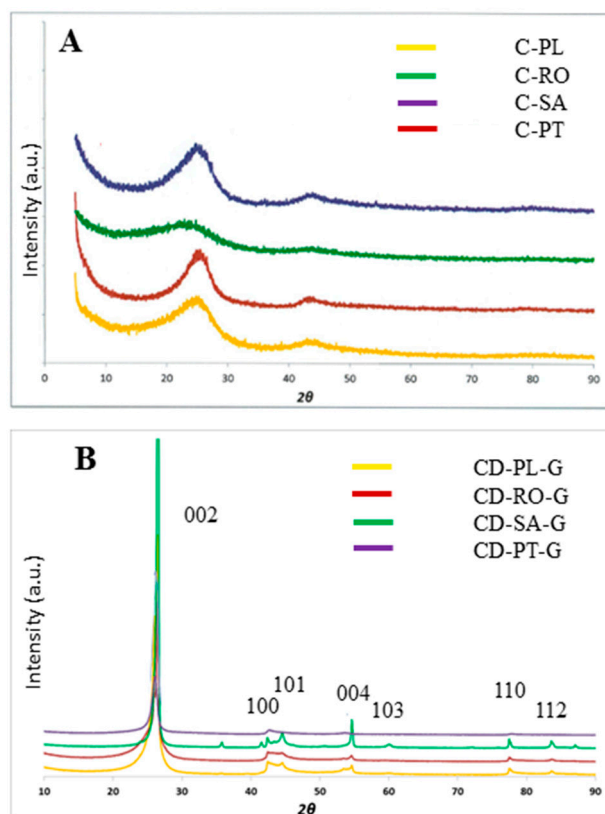n.d.—due to their highly disordered character the La was not possible to determine.

Figure 2. XRD diffractograms: (**A**) char concentrates from Poland (C-PL), Romania (C-RO), South Africa (C-SA), and Portugal (C-PT); (**B**) graphitized demineralised char concentrates from Poland (CD-PL-G), Romania (CD-RO-G), South Africa (CD-SA-G), and Portugal (CD-PT-G).

In ideal graphite, the d_{002} is 0.3354 nm, and in turbostratic (random) graphite, the d_{002} is 0.3440 nm [66]. Based on these limits, all the char concentrate samples ($d_{002} > 0.3440$ nm) are classified as turbostratic graphite and have a turbostratic structure [14]. When considering the crystallite sizes, the L_c values for the char concentrates are small, especially when compared to the reference natural graphite sample, where the L_c value is above 30 nm. Due to the highly diffused diffractograms of the char concentrates, the L_a values could not be determined. In terms of the number of aromatic layers (<N>), the char concentrates have between 3 and 5 graphene layers in each graphite crystal. Carbonaceous material can be classified as coaly, disordered graphite, graphite, or fully-ordered graphite based on their d_{002} and L_c values (Figure 3) [67]. In this study, the char concentrates are all classified as coaly material.

Concerning the Raman microspectroscopy results, the first order graphite band (G) and four defect bands (D1-D4) are present in the char concentrate samples, while the second-order bands are diffused (Figure 4). The D1/G FWHM ratio is large (Table 5), and these characteristics indicate a disorder. Three types of spectra, labelled A, B, and C in Figure 4 and Table 5, were observed in the char concentrate samples. Type A was observed in all the char concentrate samples, and following Kouketsu et al. [68], this spectrum type indicates the presence of transitional carbonaceous material. This means the samples have characteristics ranging between amorphous carbon and graphite. Types B and C were observed only in the C-RO sample, and following Kouketsu et al. [68], these spectra indicate the presence of highly disordered amorphous carbonaceous material.
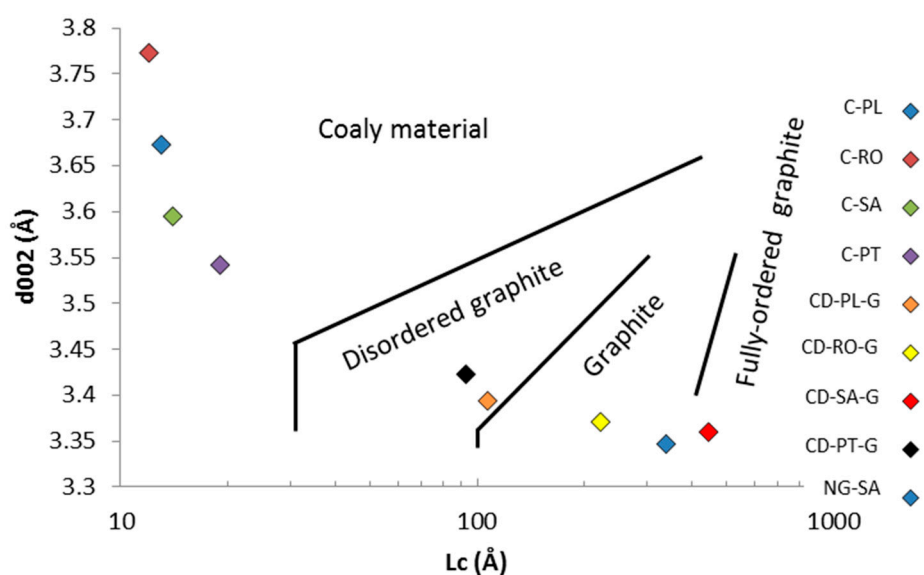
Figure 3. Classification of carbonaceous material (modified from Tagiri and Oba [67]).
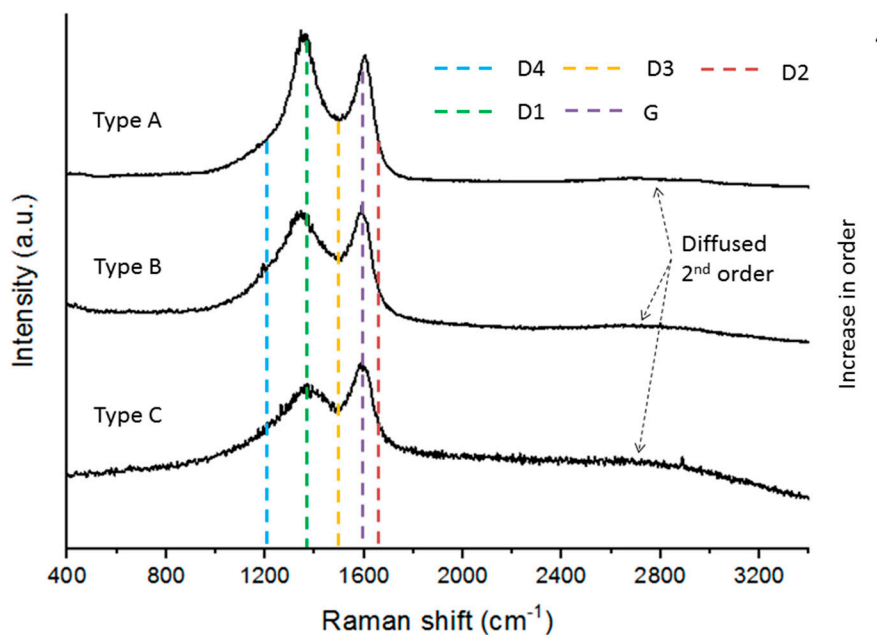

Figure 4. Raman microspectroscopy spectra determined in the char concentrates. Type A was observed for C-PT, C-PL, C-SA, and C-RO; types B and C were only observed in C-RO (G—Graphite band, D—Defect band).

The SEM/EDS analysis on the char concentrates reveals differences in the predominant char types of each sample. The terminology used to describe the features combines terminology from Vleeskens et al. [69,70], Menendez et al. [71], and Valentim et al. [72]. A representative image of each char concentrate is shown (Figure 5). Massive char particles with perforated walls and many char particles with smoother surfaces exhibiting plastic flow features around the pores were observed in C-PL (Figure 5A). The char particles in C-PT are mainly rounded and porous with perforated thin walls, and the secondary vacuoles at the surface are commonly filled by micrometric (<10 μm) aluminosilicate glassy spheres (Figure 5B). The C-RO sample differs from the other three with a predominance of massive and edgy char particles (Figure 5C), and gypsum and framboidal pyrite were found in this sample (Figure 6). A significant number of irregularly shaped inertinite-derived char particles were

observed in the C-SA char concentrate (Figure 5D). Aluminosilicate glass and quartz were found within the char structure in C-PL and C-SA (Figure 7).

Table 5. Raman microspectroscopy curve fitting results (FWHM—Full width at half maximum, I_t—Intensity ratio).

Char Concentrates			
Calculated Curve Fitting Parameters	**TYPE A**	**TYPE B**	**TYPE C**
G-D1 distance (cm^{-1})	232.50 ± 4.52	222.98 ± 3.47	214.07 ± 3.94
$\frac{D1}{G}$ FWHM ratio	1.39 ± 0.10	1.54 ± 0.08	1.62 ± 0.12
$\frac{D1}{G}$ area ratio	1.62 ± 0.10	1.31 ± 0.08	1.27 ± 0.15
RA1	0.58 ± 0.02	0.56 ± 0.02	0.57 ± 0.03
RA2	1.41 ± 0.11	1.29 ± 0.08	1.31 ± 0.13
Graphitized Demineralised Char Concentrates			
Calculated Curve Fitting Parameters	**TYPE A**	**TYPE B**	**TYPE C**
I_t	0.57 ± 0.01	0.53 ± 0.02	0.46 ± 0.01
	TYPE D	**TYPE E**	**TYPE F**
I_t	0.42 ± 0.01	0.380.02	0.25 ± 0.00
Natural Graphite Reference Sample			
Calculated Curve Fitting Parameters	**NG-SA**		
I_t	0.65		
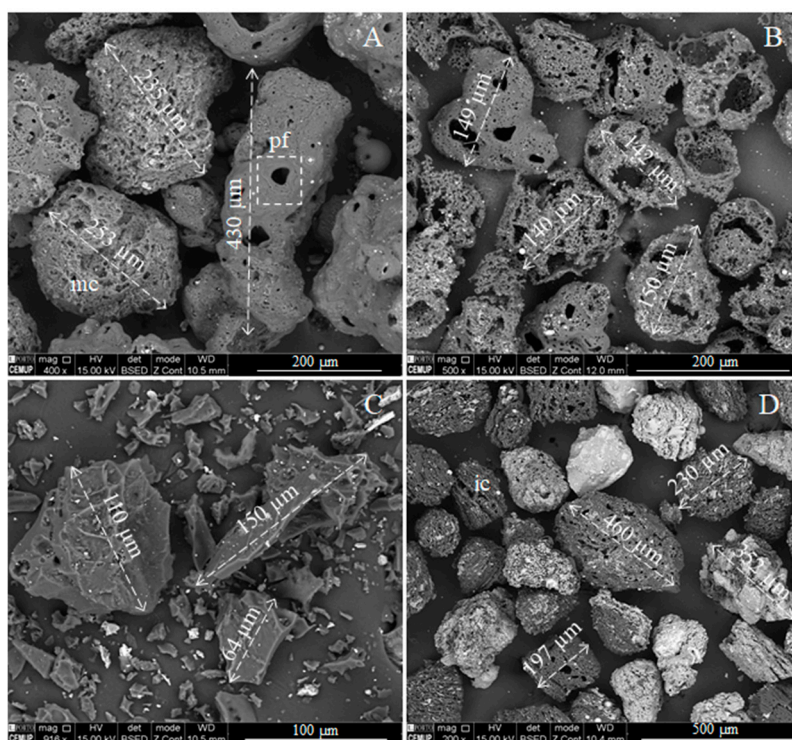
Figure 5. Char concentrates: (**A**) Poland (C-PL), massive char (mc) and a char particle exhibiting plastic flow (pf) around pores (×400; BSE mode); (**B**) Portugal (C-PT), rounded and porous char with perforated thin walls (×500; BSE mode); (**C**) Romania (C-RO), massive edgy char particles (×916; BSE mode); (**D**) South Africa (C-SA), significant number of irregular shaped inertinite derived char particles (ic) and large glassy particles (×200; BSE mode).
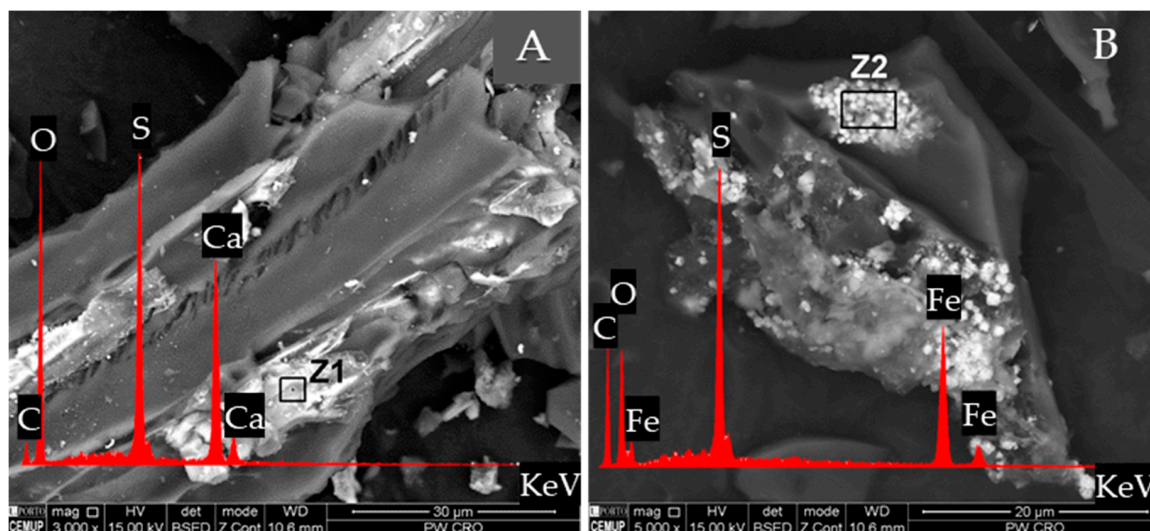
Figure 6. Mineral matter in the Romanian char concentrate sample (C-RO): (**A**) gypsum (×3000; BSE mode); (**B**) pyrite (×5000; BSE mode).
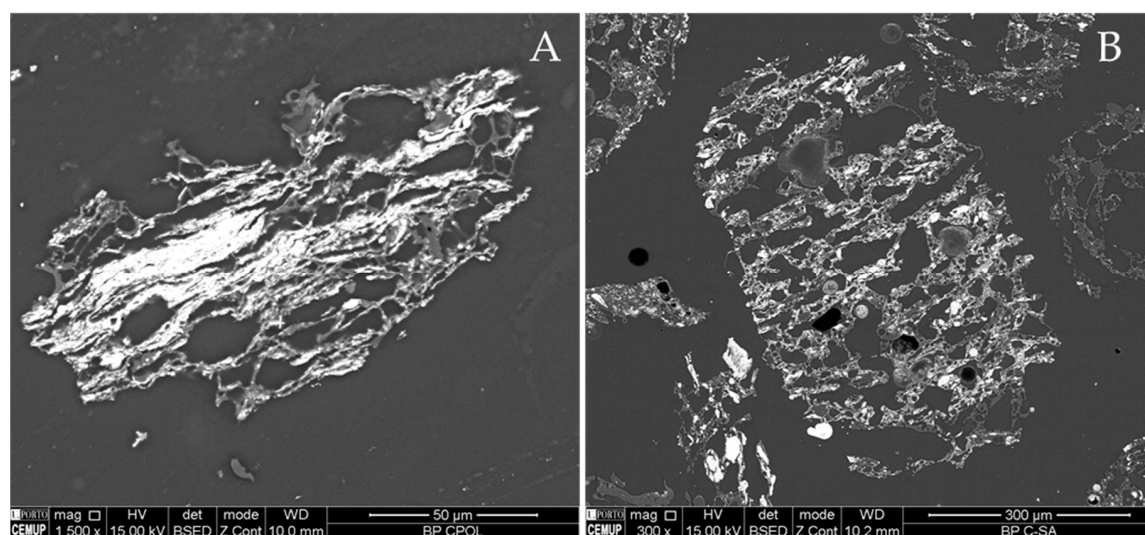

Figure 7. Char particles with mineral matter in its structure, mainly aluminosilicates: (**A**) Polish char (C-PL) (×1500; BSE mode); (**B**) South African char (C-SA) (×300; BSE mode).

The morphology of the char concentrate samples (Table 6), as determined petrographically, shows the C-SA sample is dominated by anisotropic and inertinite chars (mixed porous chars 40.4%); the C-PL sample is dominated by anisotropic chars (tenuinetworks and crassinetworks), and; the C-PT sample is dominated by anisotropic chars (83.3%) (tenuispheres and crassispheres). The C-RO sample contains a significant portion of unreacted particles and mixed porous chars.

Table 6. Quantitative morphology results of the char concentrates (ICCP—International Committee for Coal and Organic Petrology).

	Petrography (vol. %)	C-PT	C-PL	C-SA	C-RO
Hower Classification [57]	Glass	5.0	8.2	5.8	4.2
	Anisotropic char	83.3	57.8	43.2	0.6
	Isotropic char	9.5	24.0	15.6	46.4
	Inertinitic char	2.2	9.8	35.0	3.6
	Unreacted/partially burned coal	0.0	0.2	0.4	45.2
ICCP Classification [58]	Tenuisphere	17.9	0.0	0.0	0.2
	Crassisphere	34.6	7.1	0.0	0.0
	Tenuinetwork	14.3	26.0	2.9	8.5
	Crassinetwork	18.4	31.3	23.3	24.2
	Mixed porous	7.8	23.2	40.4	32.6
	Mixed dense	0.0	2.8	22.4	11.7
	Inertoid	0.5	0.6	5.5	2.7
	Fusinoid/solid	1.7	1.5	3.9	14.9
	Mineroid	4.8	7.5	1.6	5.2

3.2. Characterisation of Demineralised Char Concentrates

Due to the large percentage of inorganic matter in the char concentrates, the char concentrates were demineralised before the carbonisation–graphitization trials. Inorganic matter will clog the graphitization furnace rendering graphitization impractical. To examine the effect of the demineralisation, proximate, XRF, ss-NMR, and SEM/EDS analyses were conducted on the demineralised samples.

The proximate and XRF data are provided in Table 7. The carbon content increased in the CD-PL, CD-PT, and CD-SA samples due to the loss of elements in silicates and carbonates, such as Si, Al, and Ca, during the acid leaching process. The CD-RO sample presents the lowest fixed carbon percentage (61.5 a.d.b. wt. %) due to its high volatile matter content (24.7 a.d.b. wt. %) but shows a relative enrichment in aluminium oxide.

Table 7. Proximate and XRF results for the demineralised char concentrates.

	Analysis	CD-PT	CD-PL	CD-SA	CD-RO
Proximate Analysis (a.d.b wt. %)	Moisture	1.3	4.2	4.4	6.6
	Ash yield	0.5	2.6	6.7	7.3
	Volatile matter	1.9	12	4.5	24.7
	Fixed carbon	96.3	81.2	84.5	61.5
XRF Analysis (wt. %)	SiO_2	0.12	0.61	0.74	<0.01
	Al_2O_3	0.14	1.23	4.22	3.63
	Fe_2O_3	0.01	0.38	0.24	0.41
	CaO	0.03	0.19	0.12	1.23
	MgO	<0.01	<0.01	<0.01	0.04
	Na_2O	<0.01	0.01	<0.01	<0.01
	K_2O	<0.01	<0.01	<0.01	0.02
	SO_3	<0.002	0.06	0.05	0.42
	MnO	<0.01	<0.01	<0.01	<0.01
	TiO_2	0.02	0.13	0.39	<0.01
	P_2O_5	<0.01	<0.01	0.05	0.03
	Cr_2O_3	<0.01	<0.01	<0.01	<0.01
	Loss on Ignition	99.47	96.91	93.97	93.81

The ^{1}H NMR signals varied between the demineralised char concentrate samples. The highest NMR signal intensities were obtained for the CD-RO and CD-PL samples, indicative of a high density of protons in these samples. In general, the proton populations can be grouped at a ^{1}H chemical shift

(δ^1H) of 7–6, 4–3, and 1–0 assigned to hydrogens corresponding to graphitic, alkoxy, and aliphatic segments in the samples. Interestingly, another unusual and strong up-field of the ^{1}H NMR signals is present at −1 to −10 ppm. The 15,16-dihydropyrene structure is the simplest example where the inner protons are highly affected for the π-electrons with a δ^1H of −5.49 ppm [73]. The NMR analysis is analogous for 15,16-dimethyl-15,16-dihydropyrene [74]. For that reason, the chemical structure of 15,16-dihydropyrene is shown in Figure 8 to represent the NMR shielding of the protonic species with a negative δ^1H in the samples.
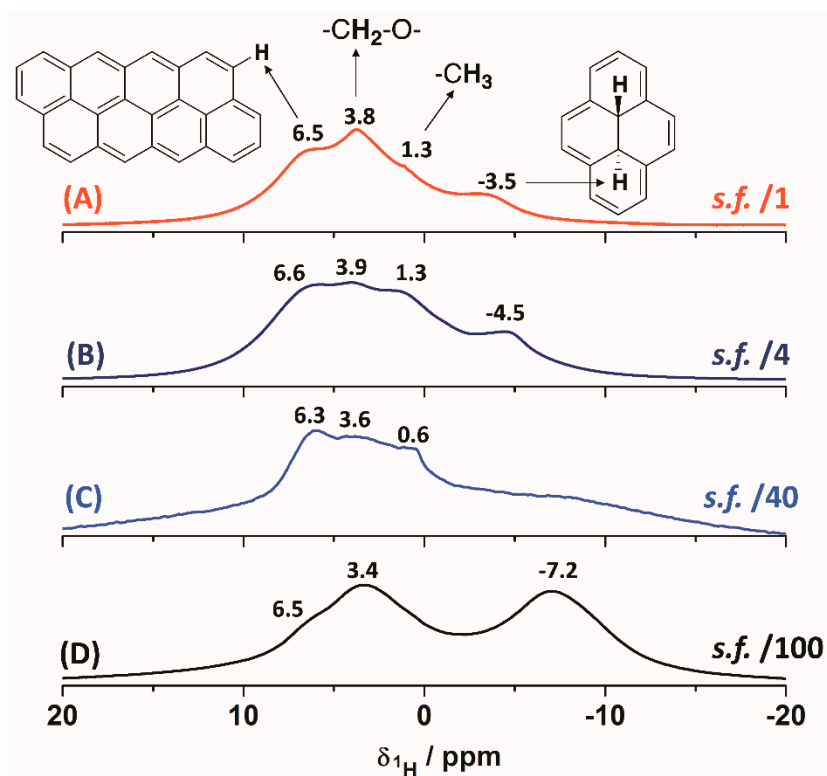
Figure 8. ^{1}H-MAS (@32 kHz) solid-state NMR spectra for the demineralised char concentrates: (**A**) CD-RO; (**B**) CD-PL; (**C**) CD-PT; (**D**) CD-SA. Scaling factors (s.f.) are indicated in each spectrum.

The behaviour was associated with the effect of the circulation of delocalised π-electrons of the graphitic structure, which reduced the local magnetic field in some protons of the samples with the concomitant shielding of the NMR signal. It is important to mention that the effect of the NMR shielding will depend on the dimension and disposition of the graphitic structures. Some authors have reported similar findings for plane and curved graphene sheets, nanotubes, and mesoporous carbon materials [75,76]. However, it is very difficult to propose a chemical representation that explains the NMR shielding of these protons (δ^1H = −1 to −10 ppm) in heterogeneous samples. For the CD-SA sample, the ^{1}H NMR signal at −7.2 represents 50% of the entire spectrum, indicative of strong interactions among the π-electrons of the aromatic rings with some of the proton of the sample [76]. A broad signal is present in the CD-PT sample at negative δ^1H, showing the high inhomogeneity in terms of chemical structure/composition for the shielded protons in this case.

The ^{13}C direct polarization spectra show that the unique signal in each sample is present at a δ^{13}C around 110–130 ppm (Figure 9); this is common in graphitic materials [77–80]. The CD-RO and CD-PL samples once again show the highest and sharpest NMR signal, related to the higher degree of order within the organic structure. The CD-SA and CD-PT samples contained mainly disordered or amorphous char according to the ^{13}C DP data. The ^{13}C CP-MAS analyses were only successful for CD-RO and CD-PL samples, considering the higher proton content observed from the ^{1}H MAS analyses.
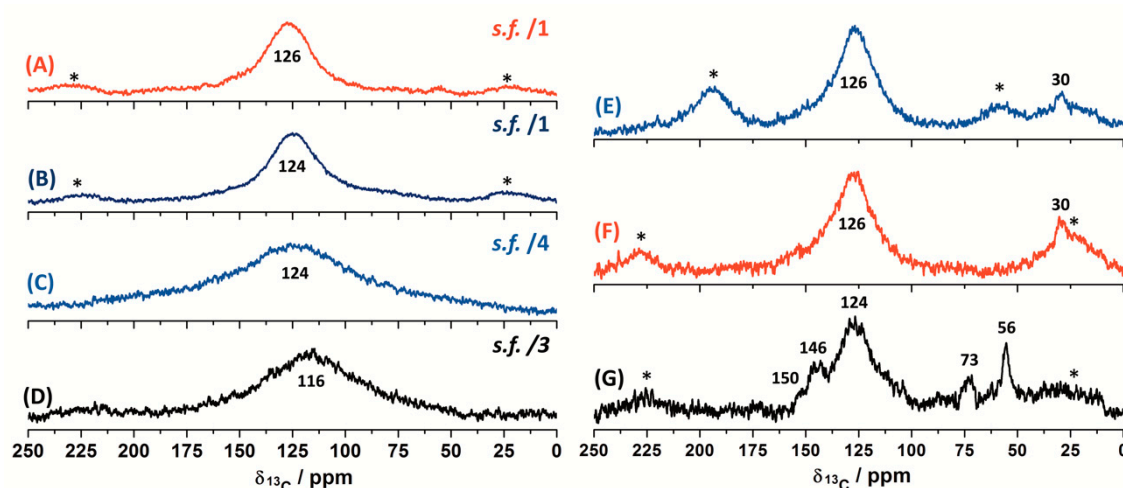
Figure 9. ^{13}C DP ss-NMR spectra (@15 kHz) for the demineralised char concentrates; (**A**) CD-RO; (**B**) CD-PL; (**C**) CD-PT; (**D**) CD-SA. Scaling factors (s.f.) are indicated in each spectrum. ^{13}C CP-MAS ss-NMR spectra for the demineralised char concentrates: (**E**) CD-PL @10 kHz; (**F**) CD-PL @15 kHz; (**G**) CD-RO @15 kHz. Spinning side bands are indicated with an asterisk.

Interestingly, the ^{13}C CP-MAS spectra were completely different, giving new insights into the sp^3 carbon content that cannot be obtained from the direct polarization analysis. Even when the ^{13}C CP-MAS data are not quantitative, the difference in the aliphatic segments was revealed. In the CD-PL sample, the main signal is the graphitic segment (sp^2 content) followed by a broad component around 40–0 ppm with a peak centred at 30 ppm ascribed to methyl or methylene groups (sp^3 content) bounded to aromatic rings. In contrast, the sp^3 content for the CD-RO sample included alkoxy carbon groups at a δ^{13}C of 73 and 56 ppm with a minority content of a broad aliphatic region at 40–0 ppm superimposed with a spinning sideband. In addition, the main component at 124 ppm for the CD-RO sample in the ^{13}C DP spectrum was resolved in three components at a δ^{13}C of 150, 146, and 124 ppm assigned to aromatic carbon with oxygen substitution, aromatic carbon with alkyl-substituted, and unsubstituted aromatic carbon together with protonated aromatic carbon, respectively [81]. Thus, the ^{13}C CP-MAS provided information at the atomic scale due to the transfer of polarization from the proton to carbon. The same graphitic and aliphatic content information was obtained from the ^{13}C CP-MAS experiments for char concentrates without demineralisation step, but the acquisition time of the NMR experiments had to be longer due to the high amount of inorganic content in these samples.

The effect of demineralisation was also determined using SEM/EDS (Figures 10–12). Limited minerals were determined for CD-PT, indicating effective demineralisation (Figure 10). However, the leaching process was not able to remove the silicates occurring deep inside the char particles for CD-PL and CD-SA, and a residue mainly composed of Al, Cl, and F also formed on the surfaces of the char particles (Figure 11). Limited visible mineral matter was noted for CD-RO, but some impurities (S, Cl, and Ca) were detected on the surface of some particles (Figure 12).
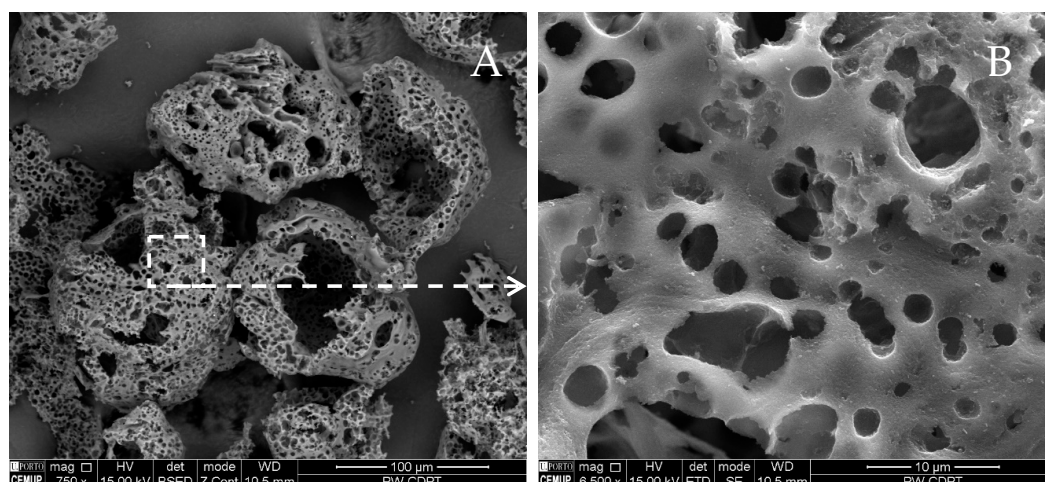
Figure 10. CD-PT: (**A**) general view (×750; BSE mode); (**B**) magnification of the empty char vacuoles (×6500; BSE mode).

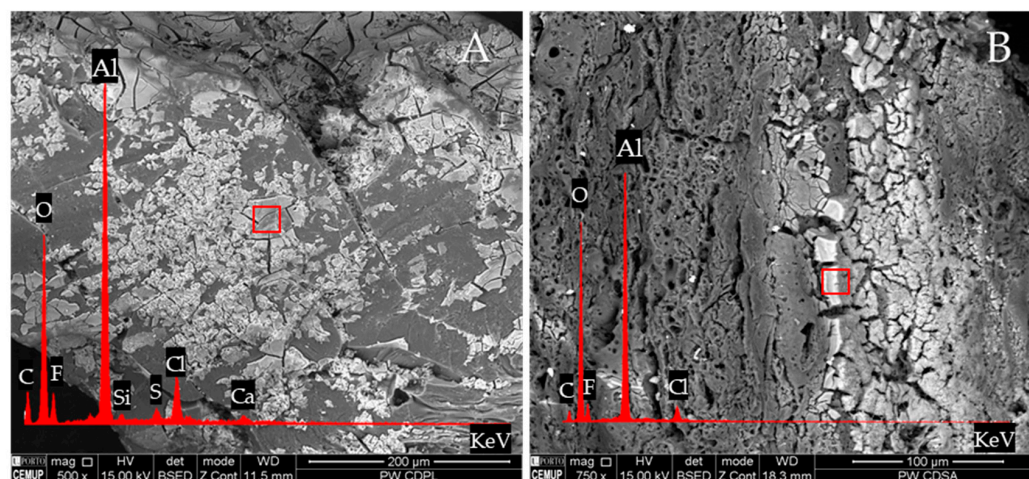**Figure 11.** Inorganic matter remaining embedded in the chars following demineralisation and the respective EDS spectra: (**A**) CD-PL (×500; BSE mode); (**B**) CD-SA (×750; BSE mode).
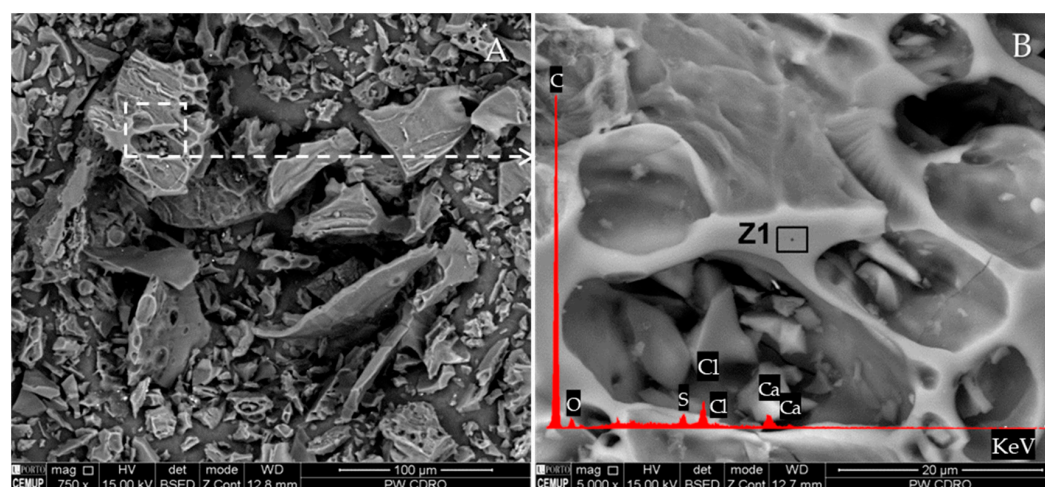

Figure 12. CD-RO: (**A**) general view with no visible mineral matter (×750; BSE mode); (**B**) magnified area and respective EDS spectrum demonstrating the presence of impurities, namely S, Cl, and Ca (×5000; BSE mode).

3.3. Characterisation of Graphitized Demineralised Char Concentrates

The graphitized demineralised char concentrates were characterised by means of XRD, Raman microspectroscopy, SEM/EDS, and petrographic analyses. The graphitized samples could not be examined using *ss*-NMR due to their magnetic susceptibilities that affect both the relaxation of the nuclei (^{1}H or ^{13}C) and the instability of the spinning of the sample at the magic angle under high power pulses during the excitation or decoupling steps [77,78,82].

The XRD diffractograms are provided in Figure 2B, and all major graphite peaks, two-dimensional and three-dimensional, emerged following graphitization of the demineralised char concentrates. The CD-SA-G sample responded the most effectively to graphitization, with well-defined (002), (004), (100), and (101) peaks. It is also the only sample presenting the (103) peak. The CD-PT-G sample appears to have less effectively graphitized, with slightly less sharpened peaks than the other samples. The d_{002}, L_c and L_a, <N>, and the GD values are provided in Table 4. The d_{002} ranges between 0.3423 and 0.3360 nm, which is smaller than the d_{002} from the char concentrates (0.3542–0.3773 nm). CD-SA-G has a d_{002} closest to the reference natural graphite while CD-PT-G is bordering the d_{002} of a turbostratic structure (0.3440 nm, [66]). The CD-SA-G has the largest graphite crystals (44.6 × 98.7 nm), while CD-PT-G has the smallest graphite crystals (9.3 × 24.4 nm). In terms of the number of aromatic layers, the graphitized demineralised char concentrates have between 27 (CD-PT-G) and 133 (CD-SA-G) graphene layers in each graphite crystal. It is much higher than the char concentrates. CD-SA-G has a degree of graphitization of 93 %, followed by CD-RO-G with 80 %, CD-PL-G with 53%, and CD-PT-G with 20%. According to the classification from Tagiri and Oba [67] (Figure 3), CD-PT-G and CD-PL-G are classified as disordered graphite, CD-RO-G is classified as graphite, and CD-SA-G as fully-ordered graphite.

This finding is supported by the Raman spectra. The first order graphite band (G) and two defect bands (D1 and D2) are present, while the D3 and D4 defect bands are near absent (Figure 13), the second-order bands are well developed (Figure 13), and the I_t ratio is small (Table 5) in the graphitized demineralised char concentrate samples. These characteristics indicate order. Six types of spectra, labelled A to F in Figure 13 and Table 5, were observed in the graphitized demineralised char concentrate samples, and following Kouketsu et al. [68], these spectra types indicate the presence of crystallised graphite. Particles exhibiting the Type F spectrum are slightly more crystallised than those exhibiting the Type A spectrum. CD-SA-G and CD-RO-G graphitized the best, with the majority of their particles classified as Type C spectra. Particles occurring as the highly ordered Types E and F are also seen in these two samples.
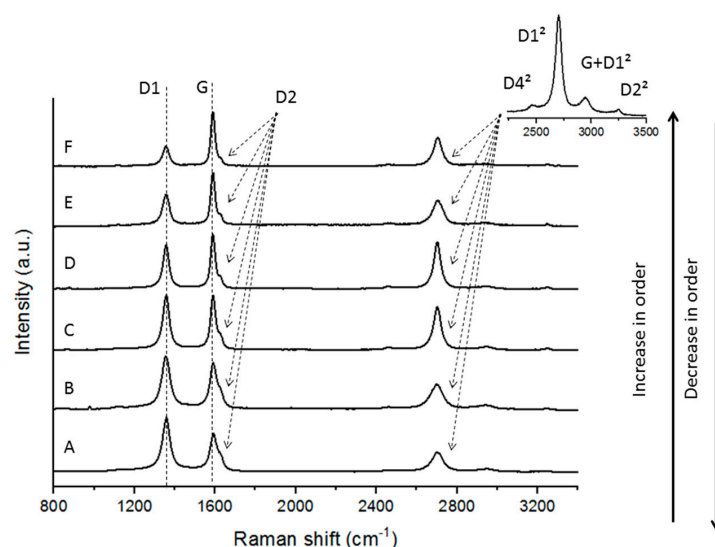

Figure 13. Raman microspectroscopy spectra determined in the graphitized demineralised char concentrates (CD-PT-G, CD-PL-G, CD-RO-G, and CD-SA-G).

The SEM/EDS and petrography analyses and observations indicate significant morphological changes (compared to the char concentrate and demineralised char concentrate samples) in the CD-RO-G, CD-SA-G, and CD-PL-G samples. The CD-PT-G sample shows limited changes following graphitization, except that the char surfaces appear to be smoother. In the CD-SA-G and CD-PL-G samples imperfect hexagonal graphite crystals were observed as discrete plates on the surface of particles (Figure 14).
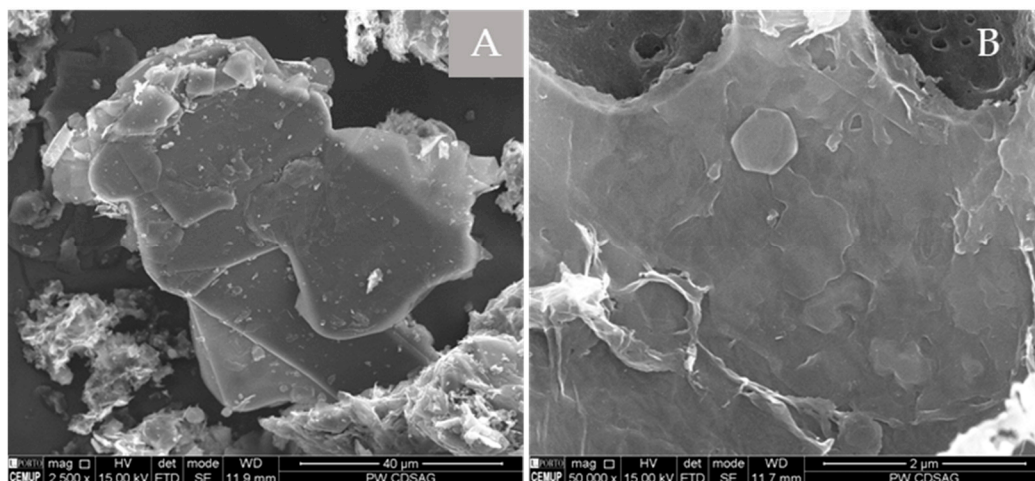

Figure 14. Examples of imperfect hexagonal graphite crystals as well as char with micromosaic walls found in: (**A**) CD-SA-G; (**B**) CD-PL-G (×2500 and ×50000; BSE mode).

A wide variety of graphite forms were observed in CD-RO-G (Figure 15), including platy, columnar, spherical, whiskers, cones, and chunk structures, which is in agreement with what is described for natural and synthetic graphite [83–91]. Some char particles present platy-structured walls (Figure 15A) suggesting a full structural reorganization during the graphitization process. Columnar graphite (stacks of graphite crystals) was found covering the inner and outer surface of carbonaceous particles (Figure 15B). The layered growth and the hollow polyhedron visible in the centre of the columnar structures suggest a macro-spiral growth, as described by Kvasnitsa et al. [83] for metamorphic graphite. The spherical morphologies appear as aggregates over the char particle surface (Figure 15C). In a single case, a hollow broken sphere with columnar structures in the inner surface was observed. The whiskers and cones were found attached to the inner and outer surface of carbonaceous particles and untied. The morphology of the whiskers varies from cylindrical with a dome-shaped tip to conical with a pointed tip, and they can reach up to 80 μm in length. Some of these structures present spiral growth steps indicating a scroll-type structure. The observation of broken whiskers and cross-sections in polished blocks show a solid structure with graphite crystals almost perpendicular to the major axis of the whiskers. These structures may have resulted from a cone-helix growth as proposed by Double and Hellawell [92]. Spherical agglomerate whiskers and cones were also observed to a lesser extent in the CD-PL-G sample. Some petrographic images are provided in Figure 16.
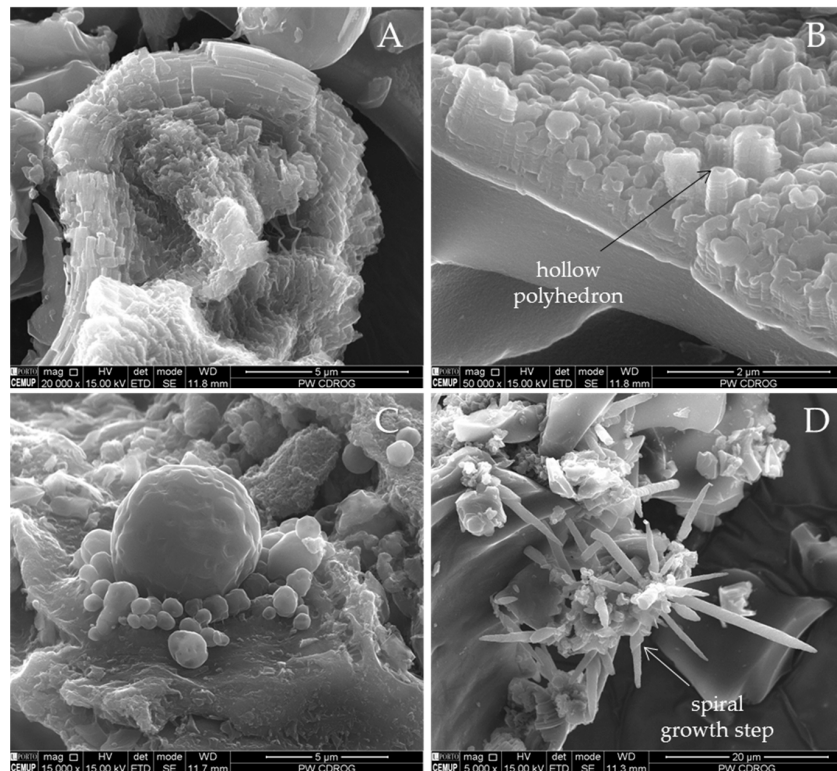
Figure 15. CD-RO-G: (**A**) char particles with walls composed by tabular graphitic material (×30,000; SE); (**B**) char particles covered with columnar graphitic material (×50,000; SE mode); (**C**) spherical agglomerates (×15,000; SE mode); (**D**) graphite whiskers (×20,000; SE mode).
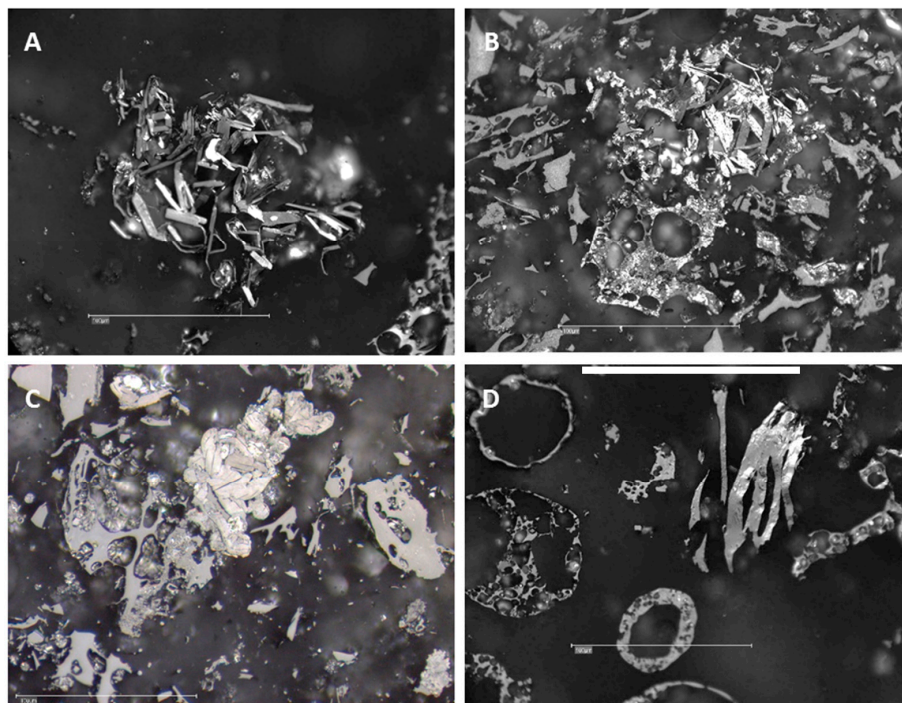

Figure 16. Particles exhibiting graphite-like texture: (**A**) CD-SA-G; (**B**,**C**) CD-RO-G; (**D**) rare graphite particles in CD-PT-G (monochrome white light, cross-polars rotated, oil immersion, scale bar = 100 µm).

3.4. Characterisation of the Reference Natural Graphite Sample

For comparison purposes, a natural graphite (flake) sample from the Goedehoop graphite deposit in South Africa (NG-SA) was characterised using XRD (Table 4), Raman microspectroscopy (Table 5), and petrography (Figure 17).
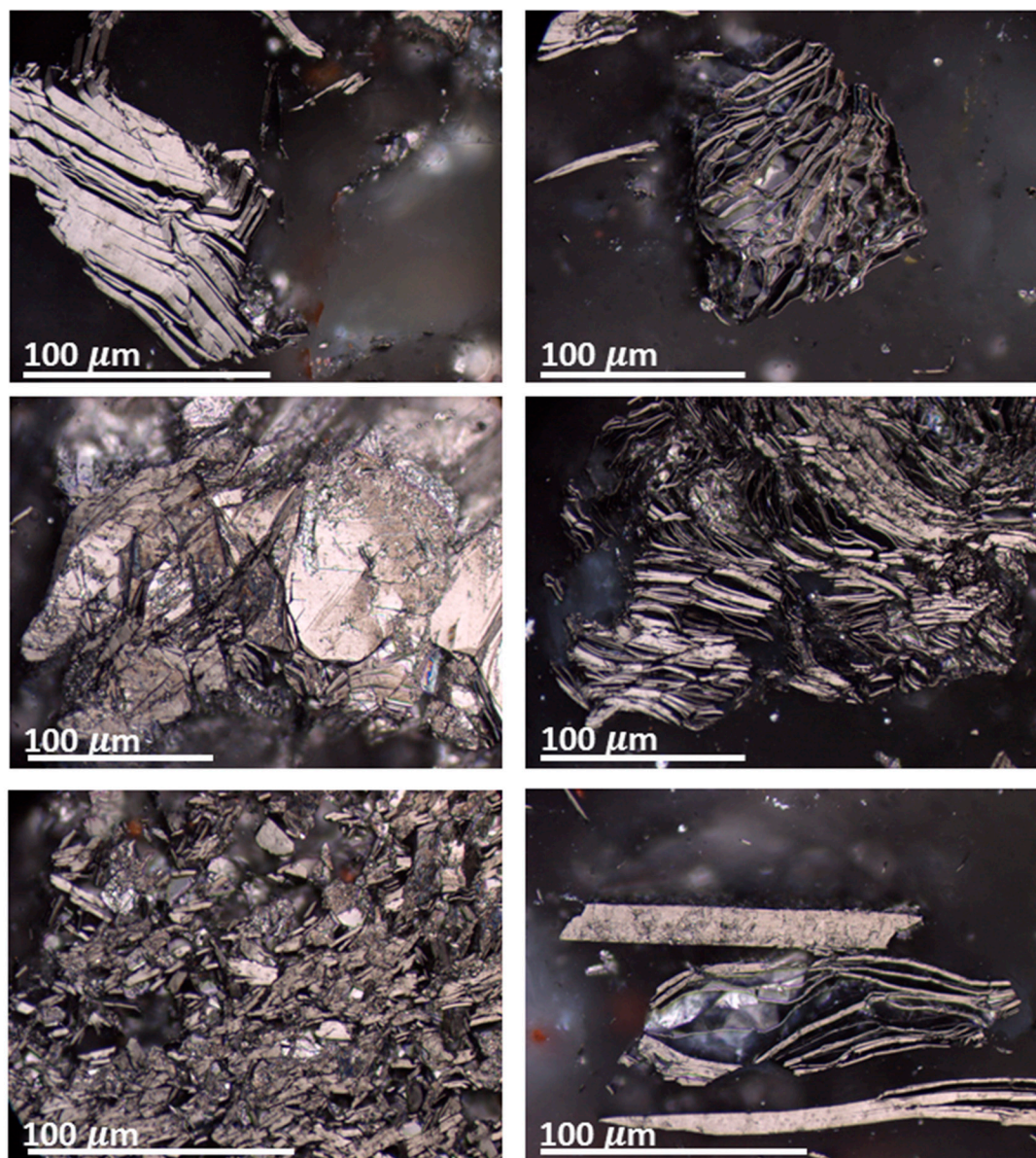
Figure 17. A collection of flake graphite particles found in the natural graphite reference sample.

The L_a value (213.2 nm) is relatively small for flake type natural graphite. According to Badenhorst [93], XRD analysis on natural graphite samples has some limitations, and quantification results should be interpreted with caution. When applying the classification from Tagiri and Oba [67] (Figure 3), NG-SA is classified as graphite. The I_t ratio for the NG-SA sample as determined with Raman microspectroscopy also classifies the sample as crystallised graphite, according to Kouketsu et al. [68].

4. Discussion

The discussion section addresses two main questions:

(1)   Was the graphitization process successful?

(2)   Which char properties most likely enhanced or hindered graphitization?

The d_{002} in ideal graphite and turbostratic graphite is 0.3354 nm and 0.3440 nm, respectively [66]. The char concentrates before graphitization presented d_{002} values ranging from 0.3542 to 0.3773 nm. After graphitization, the d_{002} decreased to a range (0.3423–0.3360 nm) that fits between the turbostratic and graphite structure. The development of crystallites over graphitization is highlighted by the differences observed in the parameters L_a and L_c. However, the size in the basal direction (L_a) from the graphitized demineralised char concentrates is far from the L_a of the reference natural graphite sample (213.2 nm). The sample CD-SA-G presents the larger crystallites in that direction, 98.7 nm. Regarding the stacking height, L_c, the CD-SA-G surpasses the reference natural graphite (33.9 nm), while the remaining sample's L_c is below 23 nm. CD-SA-G and CD-RO-G were better ordered compared to XRD structural data on graphitized anthracite [26,31,46] and char from an anthracite burning power station [21,22]. CD-PT-G, however, was highly disordered compared to the reference natural graphite and the samples from the aforementioned studies.

The Raman microspectroscopy parameter, I_t, was smaller for the graphitized demineralised char concentrates than for the reference natural graphite sample but larger than that obtained by Cabielles et al. [21,22] and González et al. [26,31,46].

The ss-NMR experiments demonstrated the presence of graphitic content in the demineralised char concentrates, at ^{13}C chemical shift of 116–126 ppm, and a higher crystallinity/order in CD-RO and CD-PL compared to the CD-SA and CD-PT where the structure was disordered/amorphous.

Morphologically, whilst some particles in each graphitized demineralised char concentrate appear to be graphitized, the samples do not meet the requirements to be classified as graphite. The CD-SA-G sample is the closest of the four, and both the CD-SA-G and CD-RO-G samples contain several graphitized particles. Hexagonal graphitized particles were observed for the CD-PL-G sample and very rare particles in the CD-PT-G sample.

The graphitization process rearranged the char structure and places it closer to the graphite ideal structure. The success of the graphitization process was different among the group of samples tested according to the subsequent order: CD-SA-G > CD-RO-G > CD-PL-G > CD-PT-G.

The degree of graphitizability also appears to be related to the inherent morphology or texture of the sample. González et al. [31] determined that samples with a lower starting anisotropic percentage lead to a better structure with a higher percentage of anisotropic particles after carbonisation, and a higher anisotropic percentage after carbonisation lead to better graphitization. This result is confirmed in the current study. The C-RO sample had a very high proportion of isotropic mixed porous char particles, and the C-SA sample, a more balanced proportion of mixed porous anisotropic and isotropic particles (Table 6). The C-PT and C-PL samples were dominated by porous anisotropic particles (83.3 and 57.8 vol. %, respectively) (Table 6). Although the number of samples is statistically limited, there is a good linear correlation between the percentage of mixed porous particles in the char concentrates and the degree of graphitization of the graphitized demineralised char concentrates (Figure 18), with an R^2 value of 0.9944 (Figure 18).

However, the graphitization degree attained, especially for CD-SA-G sample, could be related to the inorganic matter, since the demineralization of the chars was not equally efficient in all samples. This is mentioned above and illustrated in Figures 7 and 11, where it can be seen that Al-rich inorganic matter (a sort of "pulp") is still present in the char after demineralization in samples CD-PL and CD-SA, which is corroborated by the XRF analysis. The demineralization process was the same for all samples. The phenomena can be explained by the high amounts of syngenetic mineral matter in the respective coals, namely clay occurring inside fusinite (former plant ducts), which has become char inherent glassy aluminosilicate (Figure 7), making demineralization less efficient; for example, the Portuguese samples where the char is porous and almost free of inherent mineral matter.

To check the possibility that the high-amounts of Al_2O_3 in CD-PL and CD-SA played a catalytic role in the graphitizability of the char, as concluded by Cabielles et al. [21] and González et al. [26], the Al_2O_3 determined in the demineralised char concentrates and the La crystallite size of the

graphitized demineralised char concentrates were correlated (Figure 19). A linear trend exists between Al_2O_3 and La and the CD-PT-G and the CD-SA-G plots, i.e., the two extremes of Al_2O_3 amount and La size, are far from each other. However, the number of samples is statistically low and further studies are needed to confirm the effect of Al_2O_3.
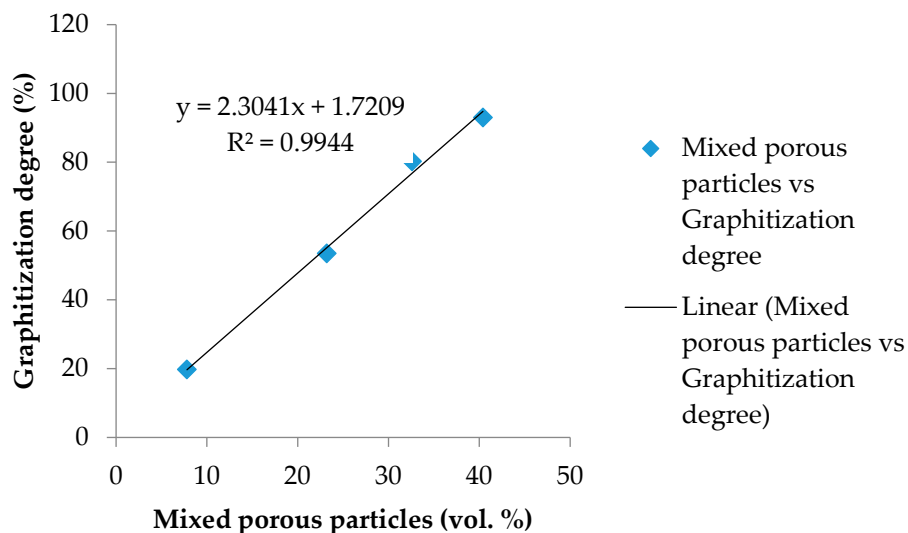

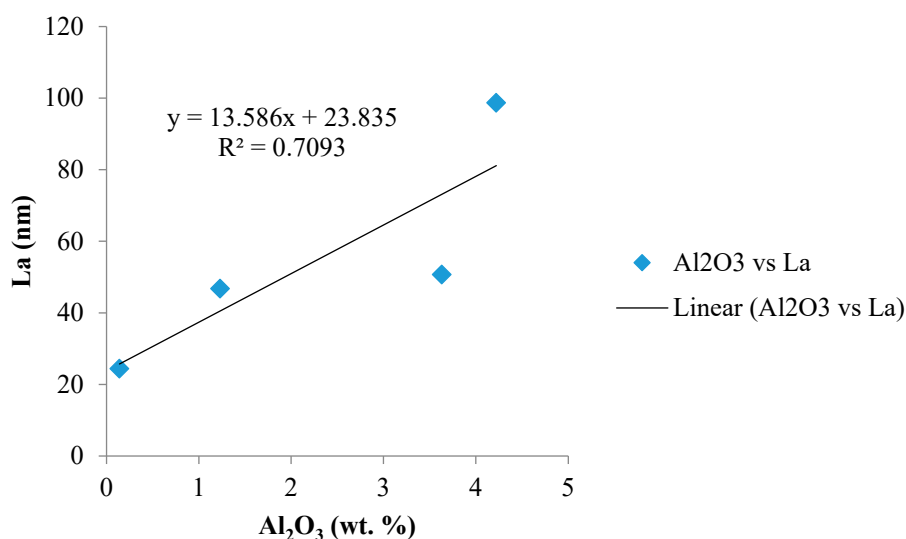**Figure 18.** Effect of mixed porous texture on the degree of graphitization.

Figure 19. Catalytic effect of Al_2O_3 minerals (mainly glass) on the crystallite growth of the basal plane.

5. Conclusions

As a whole, the synthetically graphitised char concentrates from coal fly ash and coal bottom ash are comparable to those from previous studies in which synthetic graphite was formed from secondary raw materials char and anthracite [21,22,26,31,46]. The char concentrate derived from a South African coal fly ash was the most successful of the tested samples in terms of its final degree of graphitization. This may be due to the remnant mineral matter, composed of finely embedded minerals in the char structure and Al_2O_3 remaining after demineralisation, that promoted the growth in the basal plane and improved graphitization. Texture also seems to correlate with graphitization since samples with a lower starting anisotropic percentage graphitized better than those with high anisotropic percentages. A linear trend between the amount of mixed porous particles and the graphitization degree was found.

Future work will entail the testing of the graphitized samples in green energy applications (e.g., as catalysts and as functionalized acid catalysts for levulinic acid esterification).

Conflicts of Interest: The authors declare no conflict of interest. The funders had no role in the design of the study; in the collection, analyses, or interpretation of data; in the writing of the manuscript, or in the decision to publish the results.

References

1. Harris, D.; Heidrich, C.; Feuerborn, J. Global aspects on coal combustion products. In Proceedings of the World of Coal Ash (WOCA), St. Louis, MO, USA, 13–16 May 2019.
2. Carlson, C.L.; Adriano, D.C. Environmental Impacts of Coal Combustion Residues. *J. Environ. Qual.* **1993**, *22*, 227–247. [CrossRef]
3. Fulekar, M.H.; Dave, J.M. Disposal of fly ash—An environmental problem. *Int. J. Environ. Stud.* **1986**, *26*, 191–215. [CrossRef]
4. Bartoňová, L. Unburned carbon from coal combustion ash: An overview. *Fuel Process. Technol.* **2015**, *134*, 136–158. [CrossRef]
5. Yao, Z.; Ji, X.; Sarker, P.; Tang, J.H.; Ge, L.; Xia, M.; Xi, Y. A comprehensive review on the applications of coal fly ash. *Earth Sci. Rev.* **2015**, *141*, 105–121. [CrossRef]
6. Heidrich, C.; Weir, A.; Feuerborn, H.-J. Coal combustion products: A global perspective. In Proceedings of the World of Coal Ash (WOCA), Lexington, KY, USA, 22–25 April 2013.
7. Hwang, J.; Li, Z. Control of Mercury Emissions Using Unburned Carbon from Combustion by-Products. U.S. Patent 6,027,551, 22 February 2000.
8. Hwang, J.Y.; Sun, X.; Li, Z. Unburned Carbon from Fly Ash for Mercury Adsorption: I. Separation and Characterization of Unburned Carbon. *J. Miner. Mater. Charact. Eng.* **2002**, *1*, 39–60. [CrossRef]
9. Li, Z.; Sun, X.; Luo, J.; Hwang, J.Y. Unburned Carbon from Fly Ash for Mercury Adsorption: II. Adsorption Isotherms and Mechanisms. *J. Miner. Mater. Charact. Eng.* **2002**, *1*, 79–96. [CrossRef]
10. Li, J.; Maroto-Valer, M.M. Computational and experimental studies of mercury adsorption on unburned carbon present in fly ash. *Carbon* **2012**, *50*, 1913–1924. [CrossRef]
11. Luo, J.; Hein, A.M.; Hwang, J. Adsorption of Vapor Phase Mercury on Various Carbons. *J. Miner. Mater. Charact. Eng.* **2004**, *3*, 13–22. [CrossRef]
12. Zhang, Y.; Granite, E.J.; Maroto-Valer, M.M.; Tang, Z. Activated carbons produced from unburned carbon in fly ash and their application for mercury capture. *Am. Chem. Soc. Div. Pet. Chem. Prepr.* **2003**, *48*, 32–33.
13. Baltrus, J.P.; Wells, A.W.; Fauth, D.J.; Diehl, J.R.; White, C.M. Characterization of Carbon Concentrates from Coal-Combustion Fly Ash. *Energy Fuels* **2001**, *15*, 455–462. [CrossRef]
14. Hurt, R.H.; Davis, K.A.; Yang, N.Y.; Headley, T.J.; Mitchell, G.D. Residual carbon from pulverized-coal-fired boilers. 2. Morphology and physicochemical properties. *Fuel* **1995**, *74*, 1297–1306. [CrossRef]

15. Maroto-Valer, M.M.; Zhang, Y.; Lu, Z.; Andrésen, J.M.; Schobert, H.H. Development of value-added products from fly ash carbons. In *Environmental Challenges and Greenhouse Gas Control for Fossil Fuel Utilization in the 21st Century*; Maroto-Valer, M.M., Song, C., Soong, Y., Eds.; Springer Science + Business Media: New York, NY, USA, 2002; pp. 431–444.

16. Rouzaud, J.N.; Duval, B.; Leroy, J. Coke microtexture: A key for coke reactivity. In *Fundamental Issues in Control of Carbon Gasification Reactivity*; Lahaye, J., Ehrburger, P., Eds.; Kluwer Academic Publishers: Dordrecht, The Netherlands, 1991; pp. 257–268.

17. Blanche, C.; Rouzaud, J.-N.; Dumas, D. New data on anthracite graphitizibility. In Proceedings of the 22nd Biennial Carbon Conference, San Diego, CA, USA, 16–21 July 1995.

18. European Commission. *Communication from the Commission to the European Parliament, the Council, the European Economic and Social Committee and the Committee of the Regions on the 2017 List of Critical Raw Materials for the EU*; European Commission: Brussels, Belgium, 2017; p. 8.

19. Fortier, S.M.; Nassar, N.T.; Lederer, G.W.; Brainard, J.; Gambogi, J.; McCullough, E.A. *Draft Critical Mineral List—Summary of Methodology and Background Information—U.S. Geological Survey Technical Input Document in Response to Secretarial Order No. 3359*; US Geological Survey: Reston, VA, USA, 2018; p. 26.

20. Beyssac, O.; Rumble, D. Graphitic Carbon: A Ubiquitous, Diverse, and Useful Geomaterial. *Elements* **2014**, *10*, 415–420. [CrossRef]

21. Cabielles, M.; Montes-Morán, M.; García, A.B. Structural Study of Graphite Materials Prepared by HTT of Unburned Carbon Concentrates from Coal Combustion Fly Ashes. *Energy Fuels* **2008**, *22*, 1239–1243. [CrossRef]

22. Cabielles, M.; Rouzaud, J.-N.; García, A.B. High-Resolution Transmission Electron Microscopy Studies of Graphite Materials Prepared by High-Temperature Treatment of Unburned Carbon Concentrates from Combustion Fly Ashes. *Energy Fuels* **2009**, *23*, 942–950. [CrossRef]

23. Cameán, I.; García, A.B. Graphite materials prepared by HTT of unburned carbon from coal combustion fly ashes: Performance as anodes in lithium-ion batteries. *J. Power Sources* **2011**, *196*, 4816–4820. [CrossRef]

24. Evans, E.; Jenkins, J.; Thomas, J. Direct electron microscopic studies of graphitic regions in heat-treated coals and coal extracts. *Carbon* **1972**, *10*, 637–642. [CrossRef]

25. Pappano, P.J.; Schobert, H.H. Effect of Natural Mineral Inclusions on the Graphitizability of a Pennsylvania Anthracite. *Energy Fuels* **2009**, *23*, 422–428. [CrossRef]

26. Gonzalez, D.; Montes-Morán, M.; García, A.B. Influence of Inherent Coal Mineral Matter on the Structural Characteristics of Graphite Materials Prepared from Anthracites. *Energy Fuels* **2005**, *19*, 263–269. [CrossRef]

27. Marsh, H.; Warburton, A.P. Catalysis of graphitization. *J. Appl. Chem.* **1970**, *20*, 133–142. [CrossRef]

28. Ōya, A.; Marsh, H. Phenomena of catalytic graphitization. *J. Mater. Sci.* **1982**, *17*, 309–322. [CrossRef]

29. Rouzaud, J.; Oberlin, A. Structure, microtexture, and optical properties of anthracene and saccharose-based carbons. *Carbon* **1989**, *27*, 517–529. [CrossRef]

30. Oberlin, A. Carbonization and graphitization. *Carbon* **1984**, *22*, 521–541. [CrossRef]

31. Gonzalez, D.; Montes-Morán, M.; Suarez-Ruiz, I.; García, A.B. Structural Characterization of Graphite Materials Prepared from Anthracites of Different Characteristics: A Comparative Analysis. *Energy Fuels* **2004**, *18*, 365–370. [CrossRef]

32. Suárez-Ruiz, I.; García, A.B. Optical Parameters as a tool to Study the Microstructural Evolution of Carbonized Anthracites during High-Temperature Treatment. *Energy Fuels* **2007**, *21*, 2935–2941. [CrossRef]

33. Deurbergue, A.; Oberlin, A.; Oh, J.; Rouzaud, J. Graphitization of Korean anthracites as studied by transmission electron microscopy and X-ray diffraction. *Int. J. Coal Geol.* **1987**, *8*, 375–393. [CrossRef]

34. Oberlin, A.; Terrière, G. Graphitization studies of anthracites by high resolution electron microscopy. *Carbon* **1975**, *13*, 367–376. [CrossRef]

35. Cohaut, N.; Blanche, C.; Dumas, D.; Guet, J.; Rouzaud, J. A small angle X-ray scattering study on the porosity of anthracites. *Carbon* **2000**, *38*, 1391–1400. [CrossRef]

36. Bustin, R.; Rouzaud, J.-N.; Ross, J. Natural graphitization of anthracite: Experimental considerations. *Carbon* **1995**, *33*, 679–691. [CrossRef]

37. Badenhorst, C.J.; Wagner, N.J.; Valentim, B.R.V.; Santos, A.C.; Guedes, A.; Białecka, B.; Całus, J.; Popescu, L.G.; Cruceru, M.; Predeanu, G.; et al. Char from coal ash as a possible precursor for synthetic graphite—Recent developments of the Charphite project. In Proceedings of the World of Coal Ash (WOCA), St. Louis, MO, USA, 13–16 May 2019.

38. Badenhorst, C.J.; Wagner, N.J.; Valentim, B.R.V.; Viljoen, K.S.; Santos, A.C.; Guedes, A. Separation of unburned carbon from coal conversion ash: Development and assessment of a dry method. *CCGP* **2019**, *11*, 89–96.

39. Cruceru, M.; Abagiu, T.A.; Anghelescu, L.; Diaconu, B. Study on char recovery from bottom coal ash. *Int. J. Energy Environ.* **2017**, *11*, 64–68.

40. Cruceru, M.; Diaconu, B.M.; Valentim, B.; Anghelescu, L. Possible uses of coal in circular economy. In Proceedings of the International Multidisciplinary Scientific GeoConference SGEM: Surveying Geology & Mining Ecology Management, Albena, Bulgaria, 30 June–9 July 2018.

41. Cruceru, M.; Valentim, B.; Diaconu, B.; Anghelescu, L. Procedures for recovering the residual coal from bottom ash. *Int. J. Energy Environ.* **2018**, *12*, 18–23.

42. Santos, A.C.; Guedes, A.; Bialecka, B.; Badenhorst, C.J.; Predeanu, G.; Calus-Moszko, J.; Lázaro-Martínez, J.M.; Popescu, L.; Cruceru, M.; Wagner, N.J.; et al. Recovery of carbonaceous solid residue (char) from coal ash to use as possible substitute graphite-based materials in green energy applications. In Proceedings of the World of Coal Ash (WOCA), St. Louis, MO, USA, 13–16 May 2019.

43. Wierzchowski, K.; Białecka, B.; Moszko, J.C.; Klupa, A. Characterization of unburned carbon separated from power plant slag. *Int. J. Environ. Sci. Technol.* **2020**, *17*, 2499–2510. [CrossRef]

44. Cruceru, M.; Abagiu, T.A.; Anghelescu, L.; Diaconu, B. Obtaining building materials from coal ash after separation of the residual carbon. *Int. J. Syst. Appl. Eng. Dev.* **2017**, *11*, 45–49.

45. González, D.; Montes-Morán, M.; Young, R.; Garcia, A. Effect of temperature on the graphitization process of a semianthracite. *Fuel Process. Technol.* **2002**, *79*, 245–250. [CrossRef]

46. Gonzalez, D.; Montes-Morán, M.; García, A.B. Graphite Materials Prepared from an Anthracite: A Structural Characterization. *Energy Fuels* **2003**, *17*, 1324–1329. [CrossRef]

47. ISO 11722. *Solid Mineral Fuels—Hard Coal—Determination of Moisture in the General Analysis Test Sample by Drying in Nitrogen*; International Organization for Standardization: Geneva, Switzerland, 2013; p. 5.

48. ISO 1171. *Solid Mineral Fuels—Determination of Ash*; International Organization for Standardization: Geneva, Switzerland, 2010; p. 4.

49. ISO 562. *Hard Coal and Coke—Determination of Volatile Matter*; International Organization for Standardization: Geneva, Switzerland, 2010; p. 8.

50. Laggoun-Défarge, F.; Lallier-Vergès, E.; Suárez-Ruiz, I.; Cohaut, N.; Bautista, A.J.; Landais, P.; Prado, J.G. Evolution of vitrinite ultrafine structure during artificial thermal maturation. In *Vitrinite Reflectance as a Maturity Parameter: Applications and Limitation*; ACS Symposium Series 1994; Mukhopadhyay, P.K., Dow, W.G., Eds.; American Chemical Society: Ann Arbor, MI, USA, 1994; pp. 194–205.

51. Biscoe, J.; Warren, B.E. An X-Ray Study of Carbon Black. *J. Appl. Phys.* **1942**, *13*, 364–371. [CrossRef]

52. ISO 7404-2. *Methods for the Petrographic Analysis of Coals. Part 2: Methods of Preparing Coal Samples*; International Organization for Standardization: Geneva, Switzerland, 2009.

53. Schito, A.; Romano, C.; Corrado, S.; Grigo, D.; Poe, B. Diagenetic thermal evolution of organic matter by Raman spectroscopy. *Org. Geochem.* **2017**, *106*, 57–67. [CrossRef]

54. Sforna, M.; Van Zuilen, M.A.; Philippot, P. Structural characterization by Raman hyperspectral mapping of organic carbon in the 3.46 billion-year-old Apex chert, Western Australia. *Geochim. Cosmochim. Acta* **2014**, *124*, 18–33. [CrossRef]

55. Baludikay, B.K.; François, C.; Sforna, M.C.; Beghin, J.; Cornet, Y.; Storme, J.-Y.; Fagel, N.; Fontaine, F.; Littke, R.; Baudet, D.; et al. Raman microspectroscopy, bitumen reflectance and illite crystallinity scale: Comparison of different geothermometry methods on fossiliferous Proterozoic sedimentary basins (DR Congo, Mauritania and Australia). *Int. J. Coal Geol.* **2018**, *191*, 80–94. [CrossRef]

56. Lahfid, A.; Beyssac, O.; Deville, E.; Negro, F.; Chopin, C.; Goffé, B. Evolution of the Raman spectrum of carbonaceous material in low-grade metasediments of the Glarus Alps (Switzerland). *Terra Nova* **2010**, *22*, 354–360. [CrossRef]

57. Hower, J.C. Petrographic examination of coal-combustion fly ash. *Int. J. Coal Geol.* **2012**, *92*, 90–97. [CrossRef]

58. Lester, E.; Alvarez, D.; Borrego, A.; Valentim, B.; Flores, D.; Clift, D.; Rosenberg, P.; Kwiecinska, B.; Barranco, R.; Petersen, H.; et al. The procedure used to develop a coal char classification—Commission III Combustion Working Group of the International Committee for Coal and Organic Petrology. *Int. J. Coal Geol.* **2010**, *81*, 333–342. [CrossRef]

59. Feng, B.; Bhatia, S.K.; Barry, J.C. Variation of the Crystalline Structure of Coal Char during Gasification. *Energy Fuels* **2003**, *17*, 744–754. [CrossRef]

60. Hattingh, B.B.; Everson, R.C.; Neomagus, H.W.J.P.; Bunt, J.R.; Van Niekerk, D.; Jordaan, J.H.L.; Mathews, J.P. Elucidation of the Structural and Molecular Properties of Typical South African Coals. *Energy Fuels* **2013**, *27*, 3161–3172. [CrossRef]

61. Lu, L.; Sahajwalla, V.; Kong, C.; Harris, D. Quantitative X-ray diffraction analysis and its application to various coals. *Carbon* **2001**, *39*, 1821–1833. [CrossRef]

62. Lu, L.; Kong, C.; Sahajwalla, V.; Harris, D. Char structural ordering during pyrolysis and combustion and its influence on char reactivity. *Fuel* **2002**, *81*, 1215–1225. [CrossRef]

63. Okolo, G.N. The Effects of Chemical and Physical Properties of Chars Derived from Inertinite-Rich, High Ash Coals on Gasification Reaction Kinetics. Ph.D. Thesis, North-West University, Vanderbijlpark, South Africa, 2010.

64. Van Niekerk, D.; Pugmire, R.J.; Solum, M.S.; Painter, P.C.; Mathews, J.P. Structural characterization of vitrinite-rich and inertinite-rich Permian-aged South African bituminous coals. *Int. J. Coal Geol.* **2008**, *76*, 290–300. [CrossRef]

65. Wu, S.; Gu, J.; Zhang, X.; Wu, Y.; Gao, J. Variation of Carbon Crystalline Structures and CO_2 Gasification Reactivity of Shenfu Coal Chars at Elevated Temperatures. *Energy Fuels* **2008**, *22*, 199–206. [CrossRef]

66. Franklin, R.E. The structure of graphitic carbons. *Acta Crystallogr.* **1951**, *4*, 253–261. [CrossRef]

67. Tagiri, M.; Oba, T. Hydrothermal syntheses of graphite from bituminous coal at 0.5–5 kbar water vapor pressure and 300-600.DEG.C. *J. Jpn. Assoc. Miner. Pet. Econ. Geol.* **1986**, *81*, 260–271. [CrossRef]

68. Kouketsu, Y.; Mizukami, T.; Mori, H.; Endo, S.; Aoya, M.; Hara, H.; Nakamura, D.; Wallis, S.R. A new approach to develop the Raman carbonaceous material geothermometer for low-grade metamorphism using peak width. *Isl. Arc* **2014**, *23*, 33–50. [CrossRef]

69. Vleeskens, J.; Kwiecińska, B.; Hamburg, G.; Roos, C. Identification of coal pyrolysis products by scanning electron microscopy. *Fuel Process. Technol.* **1990**, *24*, 35–43. [CrossRef]

70. Vleeskens, J.; Kwiecińska, B.; Roos, M.; Hamburg, G. Coke forms in nature and in power utilities: Interpretation with SEM. *Fuel* **1994**, *73*, 816–822. [CrossRef]

71. Menéndez, R.; Vleeskens, J.M.; Marsh, H. The use of scanning electron microscopy for classification of coal chars during combustion. *Fuel* **1993**, *72*, 611–617. [CrossRef]

72. Valentim, B.; Hower, J.C.; Guedes, A.; Flores, D. Scanning electron microscopy and energy-dispersive X-ray spectroscopy of low-sulfur coal fly ash. *Int. J. Energy Clean Environ.* **2009**, *10*, 147–166. [CrossRef]

73. Phillips, J.B.; Molyneux, R.J.; Sturm, E.; Boekelheide, V.J. Aromatic molecules bearing substituents within the cavity of the π-electron cloud—Chemical properties of trans-15,16-Dimethyldihydropyrene. *J. Am. Chem. Soc.* **1967**, *89*, 1704–1709. [CrossRef]

74. Garmshausen, Y.; Klaue, K.; Hecht, S. Dihydropyrene as an Aromaticity Probe for Partially Quinoid Push-Pull Systems. *ChemPlusChem* **2017**, *82*, 1025–1029. [CrossRef] [PubMed]

75. Gatti, G.; Errahali, M.; Tei, L.; Mangano, E.; Brandani, S.; Cossi, M.; Marchese, L. A Porous Carbon with Excellent Gas Storage Properties from Waste Polystyrene. *Nanomaterials* **2019**, *9*, 726. [CrossRef]

76. Xu, Y.; Watermann, T.; Limbach, H.-H.; Gutmann, T.; Sebastiani, D.; Buntkowsky, G. Water and small organic molecules as probes for geometric confinement in well-ordered mesoporous carbon materials. *Phys. Chem. Chem. Phys.* **2014**, *16*, 9327–9336. [CrossRef]

77. Algarra, M.; González-Calabuig, A.; Radotić, K.; Mutavdzic, D.; Ania, C.; Lázaro-Martínez, J.; Jiménez-Jiménez, J.; Rodríguez-Castellón, E.; Del Valle, M. Enhanced electrochemical response of carbon quantum dot modified electrodes. *Talanta* **2018**, *178*, 679–685. [CrossRef]

78. Algarra, M.; Moreno, V.; Lázaro-Martínez, J.M.; Rodríguez-Castellón, E.; Soto, J.; Morales, J.; Benítez, A.J. Insights into the formation of N doped 3D-graphene quantum dots—Spectroscopic and computational approach. *Colloid Interface Sci.* **2020**, *561*, 678–686. [CrossRef] [PubMed]

79. Cai, W.; Piner, R.D.; Stadermann, F.J.; Park, S.; Shaibat, M.A.; Ishii, Y.; Yang, D.; Velamakanni, A.; An, S.J.; Stoller, M.; et al. Synthesis and Solid-State NMR Structural Characterization of 13C-Labeled Graphite Oxide. *Science* **2008**, *321*, 1815–1817. [CrossRef]

80. Gao, W.; Alemany, L.B.; Ci, L.; Ajayan, P.M. New insights into the structure and reduction of graphite oxide. *Nat. Chem.* **2009**, *1*, 403–408. [CrossRef]

81. Rumpel, C.; Kögel-Knabner, I. Characterisation of Organic Matter and Carbon Cycling in Rehabilitated Lignite-rich Mine Soils. *Water Air Soil Pollut. Focus* **2003**, *3*, 153–166. [CrossRef]

82. Peixoto, A.F.; Silva, S.M.; Costa, P.; Santos, A.C.; Valentim, B.; Lázaro-Martínez, J.M.; Freire, C. Acid functionalized coal fly ashes: New solid catalysts for levulinic acid esterification. *Catal. Today*. in press. [CrossRef]

83. Kvasnitsa, V.N.; Yatsenko, V.G.; Jaszczak, J.A. Disclinations in unusual graphite crystals from anorthosites of Ukraine. *Can. Mineral.* **1999**, *37*, 951–960.

84. Dimovski, S.; Libera, J.A.; Gogotsi, Y. A Novel Class of Carbon Nanocones. *MRS Proc.* **2001**, *706*. [CrossRef]

85. Jaszczak, J.A.; Robinson, G.W.; Dimovski, S.; Gogotsi, Y. Naturally occurring graphite cones. *Carbon* **2003**, *41*, 2085–2092. [CrossRef]

86. Kwiecińska, B.; Petersen, H. Graphite, semi-graphite, natural coke, and natural char classification—ICCP system. *Int. J. Coal Geol.* **2004**, *57*, 99–116. [CrossRef]

87. Dimovski, S.; Gogotsi, Y. Graphite whiskers, cones, and polyhedral crystals. In *Carbon Nanomaterials*, 2nd ed.; Gogotsi, Y., Presser, V., Eds.; Taylor & Francis: Boca Raton, FL, USA, 2014; pp. 89–114.

88. Barrenechea, J.F.; Luque, F.J.; Millward, D.; Ortega, L.; Beyssac, O.; Rodas, M. Graphite morphologies from the Borrowdale deposit (NW England, UK): Raman and SIMS data. *Contrib. Miner. Pet.* **2009**, *158*, 37–51. [CrossRef]

89. Jaszczak, J.A.; Dimovski, S.; Hackney, S.A.; Robinson, G.W.; Bosio, P.; Gogotsi, Y. Micro- and nanoscale graphite cones and tubes from hackman valley, Kola Peninsula, Russia. *Can. Miner.* **2007**, *45*, 379–389. [CrossRef]

90. Melvin, G.J.H.; Wang, Z.; Morimoto, S.; Fujishige, M.; Takeuchi, K.; Hashimoto, Y.; Endo, M. Graphite Whiskers Derived from Waste Coffee Grounds Treated at High Temperature. *Glob. Chall.* **2019**, *3*, 1800107. [CrossRef]

91. Baer, W. Chunky Graphite in Ferritic Spheroidal Graphite Cast Iron: Formation, Prevention, Characterization, Impact on Properties: An Overview. *Int. J. Met.* **2020**, *14*, 454–488. [CrossRef]

92. Double, D.; Hellawell, A. Cone-helix growth forms of graphite. *Acta Met.* **1974**, *22*, 481–487. [CrossRef]

93. Badenhorst, H. Microstructure of natural graphite flakes revealed by oxidation: Limitations of XRD and Raman techniques for crystallinity estimates. *Carbon* **2014**, *66*, 674–690. [CrossRef]